



High-Performance Modulators Employing Organic Electro-Optic Materials on the Silicon Platform

Wolfgang Freude , *Life Senior Member, IEEE*, Alexander Kotz , Hend Kholeif , Adrian Schwarzenberger , Artem Kuzmin , Carsten Eschenbaum , Adrian Mertens , Sidra Sarwar , Peter Erk, Stefan Bräse , and Christian Koos , *Member, IEEE*

(Review Paper)

Abstract—Silicon photonic integrated circuits comprising electro-optic modulators are key to a broad spectrum of applications. However, while the silicon photonics platform takes advantage of the well-established complementary metal-oxide-semiconductor (CMOS) processing technology for fabricating silicon-on-insulator (SOI) waveguides with high reproducibility, crystalline silicon lacks a second-order nonlinear susceptibility, which limits the functionality of the entire integration platform. The plasma dispersion effect provides an alternative means to change the refractive index by injection or depletion of carriers, but this approach has some disadvantages with respect to speed, efficiency, and footprint. Complementing silicon with Pockels-type

organic electro-optic materials (silicon-organic hybrid, SOH) can overcome these limitations. In this review, we describe state-of-the-art organic electro-optic materials, address promising strategies to resolve stability concerns, discuss fabrication technologies, and we elaborate on the design of SOH Mach-Zehnder modulators (MZM). Our discussion on performance and applications of SOH MZM starts with the definition of metrics by which various modulator realizations can be compared. Beyond the standard use of SOH MZM, we draw attention to unconventional applications like optical read-out of cryoelectronic circuits and other emerging areas in metrology and sensing which are so far not in the primary focus of the community.

Index Terms—Electro-optic modulator, Mach-Zehnder modulator (MZM), organic electro-optic materials, silicon photonics, photonic integrated circuits.

I. INTRODUCTION

SILICON is the preferred material for fabricating photonic integrated circuits (PIC) [1]. One of the key components of PIC are electro-optical (EO) modulators. Because crystalline silicon has a centrosymmetric lattice structure and therefore lacks an EO effect (second-order susceptibility $\chi^{(2)} = 0$), silicon photonics modulators conventionally exploit free-carrier dispersion through injection or depletion of charge carriers in *pin*-diode or metal-oxide-semiconductor (MOS) structures [3]. Incorporated within optical waveguides and controlled by a drive voltage, such structures change the local refractive index and therefore the optical phase of a propagating guided mode, while also influencing the optical amplitude as a side effect. If such a phase shifter (PS) region is part of a ring resonator coupled to a bus waveguide, a tunable notch filter is formed: The PS changes the resonance frequency of the ring, and therefore the transmission through the bus waveguide can be modulated [3].

If the electrically driven PS regions are part of one or both arms of a Mach-Zehnder interferometer (MZI), a Mach-Zehnder modulator (MZM) results [2], [3]. For carrier-injection phase shifters relying on forward-biased *pin*-junctions, the injected carriers can populate a significantly large fraction of the waveguide cross-section, resulting in a strong phase shift [4]. Therefore the PS sections can be kept short ($L = 200 \mu\text{m}$). However, the slow recombination dynamics of minority carriers under forward bias limits the modulation bandwidth to about $f_{\text{EO } 3\text{dB}} = 1 \text{ GHz}$, and only with a pre-emphasis the modulation speed of 10 Gbit/s

Manuscript received 31 October 2023; revised 17 March 2024; accepted 26 March 2024. Date of publication 4 April 2024; date of current version 7 June 2024. This work was supported in part by the European Research Council (ERC Consolidator Grant “TeraSHAPE” under Grant 773248, in part by the EU project “TeraSlice” under Grant 863322, in part by the Deutsche Forschungsgemeinschaft (DFG, German Research Foundation) through projects PACE under Grant 403188360 and GOSPEL Grant 403187440, through the DFG Collaborative Research Center (CRC) HyPerion, SFB 1527 Grant 454252029, through the Excellence Cluster 3D Matter Made to Order under Grant EXC-2082/1 – 390761711, in part by the BMBF projects Open6GHub under Grant 16KISK010 and INTERSOUL Grant 16KISK244K, in part by the Karlsruhe School of Optics & Photonics (KSOP), and in part by the Alfried Krupp von Bohlen und Halbach Foundation. (Corresponding author: Wolfgang Freude.)

Wolfgang Freude, Alexander Kotz, Hend Kholeif, Adrian Schwarzenberger, and Artem Kuzmin are with the Institute of Photonics and Quantum Electronics (IPQ), Karlsruhe Institute of Technology (KIT), 76131 Karlsruhe, Germany (e-mail: w.freude@kit.edu; alexander.kotz@kit.edu; hend.kholeif@kit.edu; adrian.schwarzenberger@kit.edu; artem.kuzmin@kit.edu).

Carsten Eschenbaum and Adrian Mertens were with the Institute of Photonics and Quantum Electronics (IPQ), Karlsruhe Institute of Technology (KIT), 76131 Karlsruhe, Germany. They are now with the SilOriX GmbH, 76131 Karlsruhe, Germany (e-mail: c.eschenbaum@silorix.com; adrian.mertens@partner.kit.edu).

Sidra Sarwar is with the Institute of Microstructure Technology (IMT), 76131 Karlsruhe, Germany, and also with the Institute of Organic Chemistry (IOC), both KIT, 76131 Karlsruhe, Germany (e-mail: sidra.sarwar@kit.edu).

Peter Erk is with the erConTec GmbH, 67157 Wachenheim, Germany, also with the Karlsruhe Institute of Technology (KIT), 76131 Karlsruhe, Germany, and also with the SilOriX GmbH, 76131 Karlsruhe, Germany (e-mail: peter.erk@partner.kit.edu).

Stefan Bräse is with the Institute of Organic Chemistry (IOC), 76131 Karlsruhe, Germany, and also with the Institute of Biological and Chemical Systems – Functional Molecular Systems (IBCS-FMS), both KIT, 76131 Karlsruhe, Germany (e-mail: stefan.braese@kit.edu).

Christian Koos is with the Institute of Photonics and Quantum Electronics (IPQ), 76131 Karlsruhe, Germany, also with the Institute of Microstructure Technology (IMT), both KIT, 76131 Karlsruhe, Germany, and also with the SilOriX GmbH, 76131 Karlsruhe, Germany (e-mail: christian.koos@kit.edu).

Color versions of one or more figures in this article are available at <https://doi.org/10.1109/JSTQE.2024.3385375>.

Digital Object Identifier 10.1109/JSTQE.2024.3385375

can be achieved. Carrier-depletion type phase shifters [5], on the other hand, have a smaller phase shift per length. The MZM is then designed as a travelling-wave modulator [6] and requires a larger footprint ($L = 2.5$ mm) [7]. The devices usually operate in push-pull mode and are significantly faster (electro-optic limiting frequency $f_{\text{EO } 3\text{dB}} = 45$ GHz) [7] than an MZM with injection-type PS. Free-carrier dispersion modulators can be fabricated in the framework of standard complementary metal-oxide-semiconductor (CMOS) processes, but the implied constraints of the free-carrier dispersion mechanism have to be accepted.

More design freedom is possible with a different concept: Silicon-on-insulator (SOI) waveguides or even metallic plasmonic waveguides are combined with organic electro-optic materials having a significant second-order susceptibility $\chi^{(2)} \neq 0$. In the following, we refer to these concepts as silicon-organic hybrid (SOH) or plasmonic-organic hybrid (POH) integration. In contrast to silicon, nonlinear organic EO materials do neither influence the amplitude of a propagating wave, nor do they suffer from free-carrier absorption (FCA), so that they allow to construct low-loss pure phase shifters [23]. Because optical modulators are mostly used at the beginning of a transmission chain, the materials need to tolerate a reasonable amount of optical intensity. However, high optical intensities in combination with oxygen may cause photobleaching and permanent damage to the material. This can be mitigated or entirely prevented with an encapsulation [30].

For drive voltages below 1 V [24] and PS lengths around 1 mm, the interaction of the optical wave with the organic EO material is increased by using silicon slot waveguides. The EO material fills the slot, which has a width in the order of 100 nm. This SOH technology applied to MZM results in very fast modulation rates of 100 Gbit/s [8] and beyond [32], [47], [49]. Furthermore, [9] proposes a slow-light structure with slotted-waveguides filled with EO material; this technology reduces the footprint down to $L = 80$ μm while maintaining a small drive voltage of 1V.

The present review focuses on the properties of $\chi^{(2)}$ -nonlinear organic materials and on slot waveguide SOH Mach-Zehnder modulators, thereby complementing a recent article on SOH photonics [10]. The MZM come in two varieties, depending on the electrodes that apply the modulation voltage to the EO material in the PS sections: If the energy consumption is critical, then a lumped-element approach is advisable. In this case, the electrodes are electrically short and represent a capacitive load to the driving data source. If the capacitance is small enough as with plasmonic modulators, and if the drive voltage swing is sufficient [110], then the RC product of inner resistance of drive voltage source and capacitance can be quite low, leading to a very large bandwidth [79]. On the other hand, if advanced modulation formats are targeted and low drive voltages are required, a travelling-wave approach is better suited, where the electrodes form an electrical transmission line, usually in the form of a coplanar waveguide (CPW). Let aside frequency shifters [84], it is mainly for bandwidth measurement purposes that a sinusoidal radio frequency (RF) drive signal is used. Such a drive signal propagates along the CPW with an electrical phase velocity

v_{el} and modifies the optical refractive index of an optical slot waveguide through the Pockels effect. A guided optical mode experiences this electrically induced phase perturbation which propagates with the optical group velocity v_g . Electrical and optical fields have to overlap tightly for an optimum modulation efficiency, and in addition, $v_{\text{el}} = v_g$ is desired for a large modulation bandwidth. If not a sinusoidal but a data signal drives the modulator, it is basically the electrical group velocity $v_{g,\text{el}}$ which should match v_g for avoiding a bandwidth-limiting so-called “walk-off” between electrical signal and optical envelope, but mostly electrical group velocity and electrical phase velocity are not too much different.

The paper is organized as follows: In Section II, the properties of $\chi^{(2)}$ -nonlinear organic materials are discussed, the material design is explained, and we report on the long-term stability. Section III concentrates on the fabrication of the silicon structures, on deposition and protection of the organic material, and on its poling. Section IV presents various modulator designs for room temperature use, and we report on tests at elevated temperatures. Section V defines performance metrics and benchmarking results, and it reports on the use of SOH modulators in cryoelectronics; in addition, other emerging application areas for nonlinear organic materials are mentioned. Finally, we draw some conclusions.

II. PROPERTIES OF $\chi^{(2)}$ -NONLINEAR ORGANIC MATERIALS

A. Theory and Material Properties

SOH modulators rely on the Pockels effect which is shown by acentrically organized organic electro-optic materials. This means that the molecular dipoles are at least partially oriented along a preferential direction, and a macroscopic second-order susceptibility $\chi^{(2)}$ results. The dipolar molecules have electron donor and acceptor motifs covalently linked through a π -bridge (Fig. 1(a)), forming a nonlinear optical (NLO) chromophore [10], [11], [111]. Upon deposition on the SOH waveguides, these chromophores are either randomly oriented or subject to centric alignment (dipoles are arranged “head-to-tail”, no macroscopic $\chi^{(2)}$). It is crucial to translate the microscopic molecular hyperpolarizability β_{zzz} (corresponding to the macroscopic quantity $\chi_{333}^{(2)}$) in the direction of the dipole moment to the macroscopic EO coefficient (r_{33}) [12], [13], [14], established in a one-time poling process. The resulting EO coefficient (Pockels coefficient) is then given by the relation [112]

$$r_{33} = \frac{2N\beta_{zzz}(\omega)\langle\cos^3\theta\rangle g(\omega)}{n_{\text{EO}}^4}. \quad (1)$$

The quantity N denotes the chromophore concentration, g is the Lorentz-Onsager local field factor [17], [113] that corrects for partial screening of the external field, n_{EO} is the EO material’s refractive index at optical angular frequency ω , θ is the angle between input field polarization and the molecular dipole axis z , and $\langle\cos^3\theta\rangle$ (the brackets denoting the expectation value over the random orientations θ) is the average acentric order parameter, describing the orientation of the molecular dipole moment relative to the polarization of the external field. Optimization

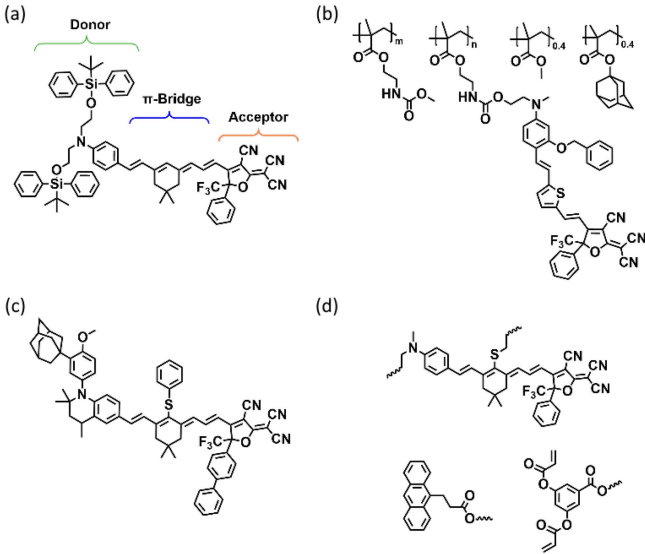


Fig. 1. Molecular structures of widely investigated EO chromophores and polymers for SOH modulators [111]. (a) JRD1. (b) Different methyl-methacrylate moieties linked to the NLO chromophore. (c) Chromophore bearing an adamantyl group for increasing T_g . (d) Thermally induced crosslinking of two NLO chromophores.

of the EO coefficient r_{33} requires simultaneous adjustment of hyperpolarizability β_{zzz} , chromophore density N , and average acentric alignment $\langle \cos^3\theta \rangle$. The factors affecting β_{zzz} are [15]

$$\beta_{zzz} \propto \frac{\Delta\mu_{eg}\mu_{ge}^2}{W_{ge}^2}, \quad (2)$$

where $\Delta\mu_{eg}$ is the difference in dipole moment between the ground and excited states, μ_{ge} denotes the transition dipole moment, and W_{ge} is the energy difference between ground and excited states (the bandgap energy). The donor and acceptor strengths increase the ground-state asymmetry and the resulting β_{zzz} values as well.

Beyond an optimal donor-acceptor match, the electron density begins to distribute symmetrically, and the molecule adopts a cyanine-like electron density distribution with $\beta_{zzz} = 0$ [16]. Lowering the optical bandgap energy W_{ge} enhances β_{zzz} . However, it is critical to avoid pushing the optical absorption towards device operating wavelengths (1310 nm or 1550 nm). State-of-the-art chromophores with high β_{zzz} commonly exhibit optical bandgaps corresponding to wavelengths of (700...1000) nm [14].

For optimizing $\langle \cos^3\theta \rangle$, an electric-field poling procedure [17], [18] is used to align the chromophores acentrically. This process involves first heating the EO material near its glass transition temperature T_g to increase the mobility of molecules, followed by the application of an external electric field to align the dipolar molecules. After cooling the material to ambient temperature while maintaining the electric field, the desired orientation of the material is preserved. Sections III-B and IV-A provide more detailed and practically oriented descriptions of the poling process.

During the previous three decades, NLO organic materials with large β_{zzz} -values have been developed intensively, but

the majority of them were not specifically optimized for SOH modulators [14], [19], [20].

B. Material Design

The current focus of research in electro-optic chromophores is to develop materials with high r_{33} -values, low optical loss, high thermal stability, and persistent acentric alignment [21], [22]. Advances in molecular engineering led to chromophores such as JRD1 (Fig. 1(a)) demonstrating excellent performance in SOH modulators [23], [24], [111] (low half-wave voltage-length products $U_{\pi}L$ and high modulation bandwidths $f_{EO\ 3dB}$). However, molecular re-orientation of dipoles after a certain period of time still leads to long-term stability issues in many of these materials. The relaxation rate to a centric alignment is closely related to the mobility and hence to the glass transition temperature T_g of the material. Therefore, T_g of the EO material and of the associated polymer matrix should be significantly higher than the operating temperature to maintain the acentric order.

Different approaches have been employed to reduce thermally induced relaxation of macroscopically acentrically arranged NLO chromophores into an optically inactive centric or random orientation. The classical approach is to embed NLO chromophores into a polymer host matrix of polyacrylates or polycarbonates [19]. The host matrix supports the persistence of acentric order by diminishing the electrostatic interactions and by reducing molecular mobility through a higher glass transition temperature $T_g = (150 \dots 200)^\circ\text{C}$. However, the thermal decomposition temperature of NLO chromophores may restrict the choice of (very) high- T_g polymers, since poling requires heating of the material close to T_g . Furthermore, the miscibility and the solubility of polymers and chromophores in identical solvents or solvent mixtures as well as the optical properties of the host must be taken into account.

In a more sophisticated approach, NLO chromophores are covalently anchored to the backbone of a polymer or a copolymer chain which are, e.g., composed of different methyl-methacrylate moieties linked to the NLO chromophore (Fig. 1(b)). Optimization of these copolymeric structures and a successive enhancement of the amount of adamantyl moieties delivers a high T_g of up to 172°C [25].

Following this strategy, bulky adamantyl side groups may be covalently attached to NLO chromophores forming molecular glasses with higher T_g . Recent examples of NLO chromophores bearing one or more adamantyl groups demonstrated a T_g of up to 176°C (Fig. 1(c)) [26].

A more elaborate strategy involves thermally induced crosslinking of two NLO chromophores with complementary reactivity during the poling process, such as HLD1 with anthracene and HLD2 with acrylate groups (Fig. 1(d)). The thermally induced cycloaddition of both crosslinking units results in a 3D polymeric network that inhibits reorientation of chromophores and promises long-term stability. Such devices have also been demonstrated in SOH slot waveguide MZM [34]. However, the challenge in this approach is to control crosslinking during the poling process and to keep the main scaffold of chromophores intact [27].

There are materials containing photonically-activated crosslinking agents. So far crosslinking by light was only shown in OE thin films, and only small electro-optic coefficients up to $r_{33} = 41$ pm/V [28] were observed, (1). Moreover, no in-device studies of this type of chromophores have been performed.

C. Long-Term Stability

There is a rich variety of publications investigating the lifetime of EO chromophores in thin-film samples or in so-called bulk material. However, due to the narrow slots in the optical waveguides (WG) of an SOH device, the chromophores are exposed to especially high optical intensities, and the resilience of promising materials to photochemical bleaching needs to be tested and verified with in-device experiments. Another source of lifetime limitation is operation at a temperature close to the glass transition temperature T_g , leading to depoling because the acentric order of chromophores is lost. Both effects increase the so-called half-wave voltage U_π which specifies the drive voltage for which the phases of the two MZM arms are offset by π . For a given phase-shifter length L , a smaller U_π implies a larger modulation sensitivity. Usually, the product $U_\pi L$ is specified.

In the following, we focus on studies investigating the in-device lifetime of EO organic materials due to bleaching and elevated temperatures.

Photochemical bleaching: The exposure of an SOH device to oxygen in combination with high optical intensities irreversibly damages the EO material, and the half-wave voltage U_π of the modulator increases [29]. Photochemical bleaching can be avoided by an oxygen-blocking encapsulation, as is already done in the OLED industry (organic light-emitting diode). First results of the long-term stability of an encapsulated POH device with respect to photochemical degradation have been already shown [30].

Thermal depoling: If the device's operating temperature is close to the T_g of the organic EO material, it depoles, resulting in an increase of the half-wave voltage U_π . Only for non-crosslinked materials, this thermal depoling is reversible, and the device could be poled again. However, because it is impractical to repole a modulator during operation, developing EO materials with high thermal stability is required and therefore an active area of research. In general, photonic devices should adhere to the industry Telcordia standard [31], which details the requirements with respect to reliability. The targeted maximum operating temperature according to this standard is 85 °C.

Long-term stability experiments: A first study of the long-term stability of an SOH MZM [22] investigated an EO material with a bulky adamantly sidegroup (Fig. 1(b)). In the study [25] discussed here, four devices were stored in an oven at a temperature of 85 °C for 2700 hours. The half-wave voltage U_π was measured repeatedly during storage. The lowest initial $U_\pi L$ of all devices was 2.22 Vmm. The degradation of U_π during the measurement can be seen in Fig. 2(a). On average, U_π increased by 45%. Notably most of the degradation takes place in the first few hundred hours, which can be considered a burn-in time, in which the device reaches a stable π -voltage level.

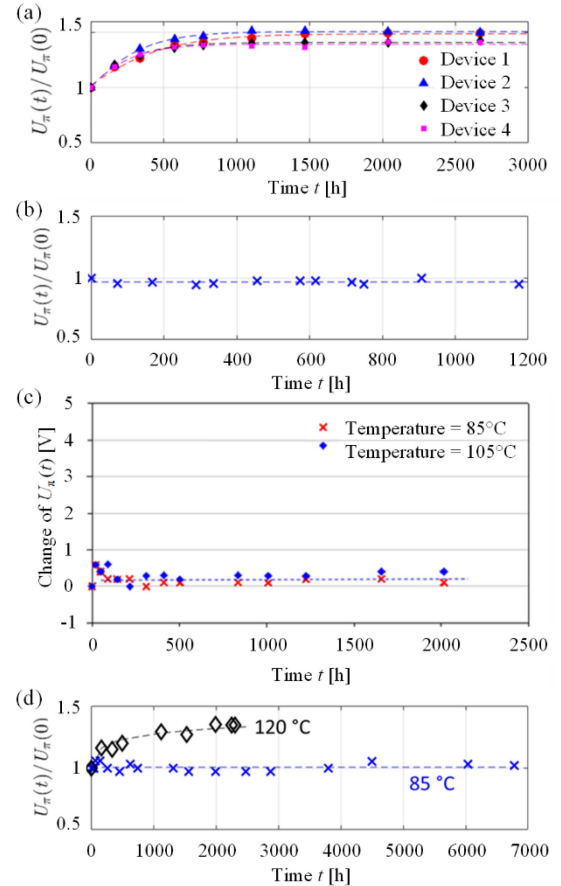


Fig. 2. Storage stability of SOH and SPH (silicon-polymer hybrid (SPH), see Section IV-C) MZM with different EO materials at elevated temperatures. (a) U_π of four SOH MZM as a function of time normalized to their initial value. The devices used an EO material with a T_g of 172 °C. They were stored at 85 °C and ambient atmosphere. After an initial burn-in time, the value U_π settles to on average of 1.45 times its initial value. (Figure adapted from [25]) (b) Normalized U_π over time of an SOH MZM with Perkinamine™ Series 5A. The half-wave voltage U_π remains constant for 1200 hours of thermal storage at a temperature of 85 °C in vacuum. (Figure adapted from [32]) (c) Thermal stability of an SPH MZM featuring the organic material EO194. Change of U_π as a function of time for devices with an initial U_π of 2.2 V. Both samples were stored in ambient atmosphere at 85 °C (red line) and 105 °C (blue line). For the device stored at 105 °C an increase of the U_π by 0.2 V was measured. (Figure adapted from [33]) (d) Thermal storage of an SOH MZM where the slots of the WG are filled with the thermally crosslinked EO material HLD. For a storage period longer than 6000 hours in vacuum at a temperature of 85 °C, no degradation of U_π could be observed. For another sample stored in vacuum at 120 °C, the device's U_π degrades to 1.3 times its initial value after 2000 hours of storage time. (Figure adapted from [34]).

A more recent study [32] demonstrated the thermal stability of a guest-host system with a T_g exceeding 175 °C. An SOH MZM with the EO material Perkinamine™ [32], mixed with amorphous polycarbonate (APC), was stored at 85 °C. No degradation was observed during 1200 hours as can be seen in Fig. 2(b). The $U_\pi L$ of the 750 μm long device was 0.46 Vmm.

Similar results are reported by industry.¹ Packaged modulators, operated at 1.55 μm during an observation time of 4300 h with an optical intensity of 0.5 MW/cm², did neither show

¹M. Lebby, "Commercializing reliable hybrid electro-optic polymer modulators," Lightwave Logic, ECOC 2 Oct. 2023. <https://www.lightwavelogic.com/presentation/ecoc-lightwave-logic-presentation-by-dr-michael-lebby/>

degradation in U_π nor in optical insertion loss. A thermal test over 2500 h at 85 °C did not reveal a significant shift in U_π .

Further, the thermal stability of silicon-polymer hybrid devices (SPH, Section IV-C, Fig. 7) featuring the materials EO173 and EO194 at temperatures of 85 °C and 105 °C was tested [33]. For a device using EO194 with a glass transition temperature $T_g = 194$ °C, the findings are depicted in Fig. 2(c). Over a period of 2000 hours, the authors measured an increase of U_π of less than 0.2 V with an initial U_π of 2.2 V. In SPH modulators, the EO material forms a 1 μm thick cladding on top of a very thin (40 nm) Si strip waveguide, leading to a comparatively high initial $U_\pi L = 22$ Vmm. The coefficient r_{33} of the EO material is reported to exceed 100 pm/V. Whether the same thermal stability and a comparably large r_{33} can be achieved in an SOH MZM with the same organic material is presently being investigated.

A different approach to increase the temperature stability of EO materials is to utilize crosslinking, a process of chemically joining two or more molecules by a covalent bond as was outlined in Section II-B.

One such material is HLD [27]. The material is made up of two molecules, namely HLD1 containing an anthracene side-group, and HLD2 containing an acrylate side-group. Prior to crosslinking, the material features a T_g of 85 °C. During the poling process, the temperature is increased to 150 °C. At these high temperatures, a network of covalent bonds forms between HLD1 and HLD2, leading to an effective increase of T_g up to 175 °C in thin films [27]. The thermal stability of crosslinked HLD (NLM Photonics Inc., Seattle, WA 98195, USA) in an SOH MZM stored at 85 °C was investigated [34]. After more than 6000 hours of storage in vacuum at a temperature of 85 °C, there was no observable degradation of U_π , blue dashed line in Fig. 2(d). In the same study, a 1 mm long device was stored at a temperature of 120 °C (black curve). During an observation time of 2200 hours, U_π increased by a factor of 1.3 from the initially measured value $U_\pi L = 1.9$ Vmm, where again most of the degradation occurred at the beginning of the test, and the π -voltage seems to reach a steady level towards the end. The high r_{33} -values of (290 ± 30) pm/V [27] achieved with crosslinked HLD for thin-film samples could so far not be reproduced in a slot waveguide.

III. FABRICATION TECHNOLOGY

A. Silicon Structure

Silicon photonics foundries specialize in designing and manufacturing silicon photonic devices. They leverage well-established silicon fabrication processes to precisely control critical dimensions, and integrate complex optical components with remarkable process stability and reproducibility. These foundries also benefit from economies of large-scale, offering cost-effective solutions for large-scale fabrication. Most foundries provide their process as a multi-project-wafer (MPW) run. In such an MPW approach, multiple photonic integrated circuit designs from users are fabricated on a single silicon wafer. For academics and fabless companies, MPW runs open a low-cost fabrication path to highly developed fabrication platforms [35].

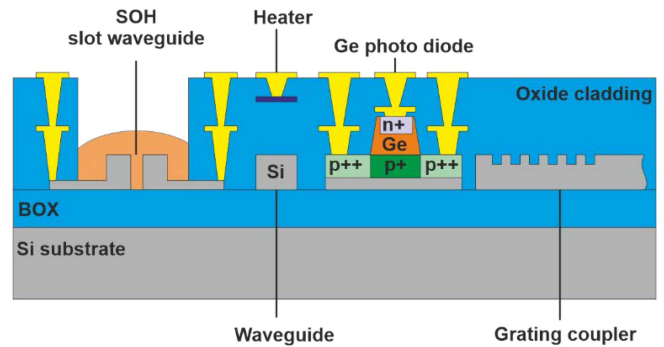


Fig. 3 Cross-sectional view of a typical multi-project wafer (MPW). The following elements are depicted (left to right, silicon regions in grey, metallic vias in yellow): Electro-optic phase shifter with SOH slot waveguide formed by silicon rails and covered with an EO organic material (orange), whereby metallic vias connect to pads on the chip's surface through which the electric drive signal is applied. Thermo-optic phase shifter with silicon strip waveguide and an associated heater. Germanium photodiode. Grating coupler for coupling outside light to an internal strip waveguide. (Figure adapted from [36]).

In the following, we briefly outline the state-of-the-art fabrication process for silicon photonic circuits, a process which is common to many foundries. Fabrication relies on silicon-on-insulator (SOI) wafers benefitting from unique advantages in terms of optical performance and integration. SOI wafers consist of a thin silicon device layer with a typical thickness of 220 nm. This layer sits on top of a (2...3) μm thick buried-oxide (BOX) layer, which provides an excellent undercladding for photonic devices, isolating the SOI waveguides from the underlying high-index handle while reducing optical losses and crosstalk. The entire chip is covered by a SiO_2 top cladding with a typical thickness in excess of 3 μm .

The fabrication process involves a series of fabrication steps, typically comprising repeated use of high-resolution deep-UV lithography with sub-100 nm resolution and overlay accuracies in the order of a few nanometers, followed by etching, deposition, or doping steps. This workflow facilitates seamless integration of photonic components with complementary metal-oxide-semiconductor (CMOS) electronics, enabling highly integrated on-chip communication systems [114].

Fig. 3 displays a schematic cross-section featuring various standard devices in a typical MPW process flow including the SOH slot waveguide. Notably, this image highlights a selective oxide opening above the phase shifter section of the SOH modulator, which enables the back end-of-line deposition of the organic EO material inside and around the slot. Electrical isolation between the two silicon rails must be ensured, and this assumes particular significance during the poling of the EO material and for the final modulator functionality.

Furthermore, Fig. 3 depicts cross-sections of basic building blocks of a typical process design kit (PDK) associated with state-of-the-art foundry service. The basic building blocks of such PDK are silicon strip waveguides with widths between 400 nm and 500 nm depending on the operating wavelength. Heaters for thermo-optic phase shifters are typically made from titanium nitride, tungsten, silicide, or doped silicon [37], and are connected via different metallization layers. Grating couplers are

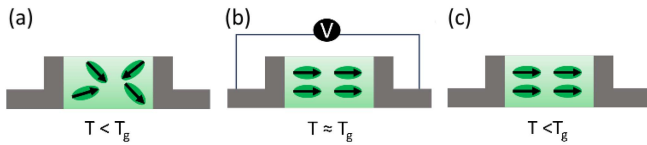


Fig. 4 Cross-section of a slot waveguide filled with an EO material (green) and poling procedure. (a) In the unpoled state, the molecular dipoles in the EO material are randomly oriented. (b) The material is heated up to its glass transition temperature T_g , and an electric field is applied to orient the dipoles. (c) The material is cooled down with the electrical field still applied, causing a “freeze in” of the orientation, even after the electrical field is shut off. (Figure adapted from [10]).

used to efficiently couple light between a planar waveguide on the silicon chip and an optical single-mode fiber or a free-space optical beam. The periodic structure etched into a waveguide diffracts the incoming light and directs it into or out of the waveguide.

Transceiver modules usually consist of transmitting and receiving components, where the receiver contains high-speed photodiodes [38], which are fabricated on the wafer by high-quality germanium growth on silicon.

For completing the silicon photonic transceiver chip, a laser light source is required. Two main approaches are commonly employed to fill this gap: Either hybridly integrating the laser on the PIC through packaging [39], [40], [115], [116], or heterogeneous on-chip integration of direct-bandgap III-V materials on silicon waveguides [117], [118].

When fabricating optical devices, especially those involving slot waveguides filled with an EO material, the precise control over locus and quantity of the material deposition is essential. The oxide opening provides a well-defined area where the EO material can be accurately deposited. The oxide opening in combination with hybridization using an EO polymer is currently not offered as a standard MPW service, but this will change in the near future.²

A more detailed cross-sectional view of the PS section of an SOH MZM comprising the electrical and the optical waveguides as well as the oxide opening is shown in the inset of Fig. 5(a).

B. EO Material Deposition, Poling and Protection

As the employed organic components are typically soluble in a plethora of solvents, massively scalable processes like inkjet-printing and micro-dispensing can be utilized for the EO-material deposition [43]. Even very simple methods like spin-coating, drop-casting or meniscus-based dispensing techniques are sufficient to build efficient devices [24], [44].

As explained in Section II, the organic EO materials of interest do not exhibit a relevant Pockels effect in their initial state, where chromophores are randomly oriented, see Fig. 4(a). The large r_{33} -values reported in literature [14], [24], [32] are achieved by orienting the molecular dipoles in a poling step, Fig. 4(b). Here, the material is heated up to its glass transition temperature T_g for

increasing the mobility of the molecules. Subsequently, a voltage is applied, creating an electric field within the slot and leading to an orientation of the respective molecules along the direction of the poling field, Fig. 4(b). This field holds the molecules in place while the material is now cooling down, leading to a “freeze-in” of the orientation at lower temperature, Fig. 4(c).

While no general parameter rules apply, the electro-optic coefficient r_{33} as a function of a poling field in the order of (200...400) V/ μm shows a threshold effect by surface-chromophore interactions, leading to alignment of chromophores along the slot sidewalls [24] [Fig. 3(b)]. This is the more pronounced the narrower the slot becomes. For higher poling fields, r_{33} reaches a maximum and then reduces due to the onset of conductance in the OE material, possibly in combination with dielectric breakdown. As discussed in Section II-C, the chromophore orientation and hence the high r_{33} coefficient will get lost if the material is again heated beyond a specific temperature without an electric field applied to the slot. Due to the confinement of the EO material within a typically $w_s \leq 200$ nm wide slot, and because of orienting effects close to the silicon side walls, the r_{33} within the device often differs significantly from the values measured in thin films [24], [32], [45].

Organic materials are usually sensitive to many environmental factors like moisture, oxygen, UV radiation, and heat [25], [29]. As discussed in Section II-C, the thermal stability of SOH devices can be achieved by utilizing EO materials with a high T_g , significantly larger than the operating temperature of the device. For mitigating the degradation due to moisture, oxygen, or radiation, the devices need to be properly encapsulated [14], [30].

IV. DESIGNS AND DEVICES

A. SOH Modulator With Resistively-Coupled (RC) Electrodes

An artistic illustration of the side-view and top-view of an SOH MZM is shown in Fig. 5(a) and (b). Light is coupled to and from the device via gratings or, alternatively, with edge-couplers (not shown). The light is guided by access waveguides to a 2×2 multimode interference (MMI) coupler where it is split into two paths. Each path is routed beneath a gap of the CPW which is tapered to the size of the probing pads for the phase shifter section. Here, a strip-to-slot (S2S) converter [46], not shown) transforms the optical mode of the strip waveguide to the slot waveguide mode that is propagating in the PS section. Filled with the EO material JRD1 [42], the insertion loss of a slot waveguide is typically 2.5 dB/mm [23]. After passing through another S2S converter at the end of the PS sections, both paths recombine in a second MMI coupler. Depending on the phase relation of the light arriving from the two arms, the light is coupled into either one or into both of the two outputs of the second MMI coupler.

The RF mode co-propagates with the optical signal along the slot WG on a metal ground-signal-ground (GSG) coplanar waveguide (yellow). The inset of Fig. 5(a) provides a schematic of the device’s slot WG cross-section. Aluminum vias punch through the (2...3) μm thick protective oxide cladding and connect the electrodes of the CPW to slabs of doped Si (typical height $h_{sb} = 70$ nm), see also Fig. 6(a). These slabs are connected to doped

²[Online available]: <https://silorix.com/announces-as-Coming-soon/>: Silicon organic hybrid MPW runs exploit SiOriX’s proprietary modulator technology along with the full portfolio of silicon photonic devices.

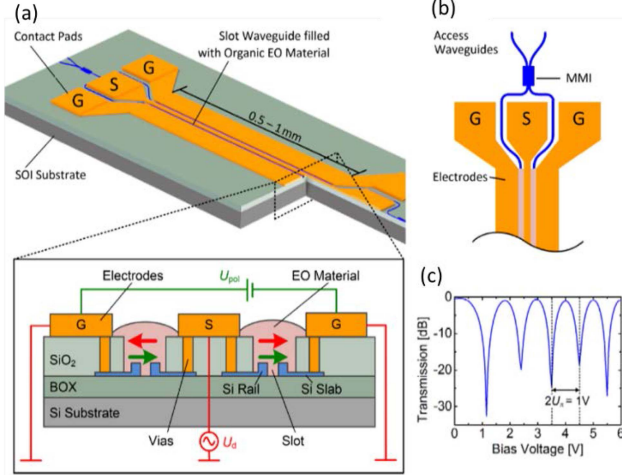


Fig. 5 Schematic of a slotted-line Mach-Zehnder modulator. (a) Electrodes in form of an RF coplanar transmission line in a ground-signal-ground (GSG) configuration. Inset: The electrodes connect to the Si rails of a slot waveguide (WG) with n -doped Si slabs (refractive index $n_{Si} = 3.5$) and to Al vias which punch through the protecting oxide. During the poling process, the EO material is heated beyond its glass transition temperature, and a direct current (DC) voltage U_{pol} (green circuit) is applied so that the chromophores align. After cooling and subsequent removing of U_{pol} , the chromophore orientation remains. A modulating voltage U_d (red circuit) applied to the signal electrode induces an electric field in the slot (red arrow) that is anti-parallel (parallel) to the chromophore alignment (green arrow) in the respective MZM arms leading to push-pull operation. Because the RF field and the optical mode overlap strongly inside the slot region, the phase modulation is highly efficient. (b) Before and after the modulator sections, the light is split and combined with multimode interference couplers (MMI). Low-loss strip-to-slot mode converters [46], not drawn) connect the MMI to the slotted PS sections which have a typical attenuation of 2 dB/mm. (c) Example of the sinusoidally-shaped MZM transmission (in dB) for PS sections with lengths $L = 1$ mm as a function of the DC bias. The half-wave voltage for a phase shift of π between both MZM arms is $U_\pi = 0.5$ V, resulting in $U_\pi L = 0.5$ Vmm. The RF modulating voltage U_d comprises a DC bias which determines the operating point, either at the null point for nearly linear amplitude modulation, or at the 3 dB point for nearly linear intensity modulation. (Figures adapted from [47], [11]).

silicon rails having typical heights of $h = (200 \dots 400)$ nm and widths of $w_{rail} = (150 \dots 240)$ nm. Both rails are separated by a slot with a width in the range of $w_s = (80 \dots 200)$ nm thereby forming the slot WG. The high index contrast at the interface between the high-index Si rail and the low-index EO material at the sidewalls of the slot leads to a field enhancement and to a strong optical confinement with a typical field interaction factor $\Gamma_{slot,x}$ of 0.18...0.25 [24], see (4), (5) in Section V-A. It is related to the modal confinement factor Γ which highly depends on the rail and slab dimensions, as well as on the slot width and the refractive index of the EO material [10], see (10) in Section V-A. A large value of $\Gamma_{slot,x}$ hence leads to a high modulation efficiency and to a small $U_\pi L$ -product.

During the poling process, the chromophores are aligned according to the electric field within the slot, induced by the poling voltage U_{pol} (Fig. 4 and green arrows in Fig. 5(a)). The modulating RF drive signal U_d is applied as shown by the red circuit in Fig. 5(a). The fields are resistively coupled from the CPW to the slot WG through the doped Si slabs. In the slot, the RF field induces an electric field (red arrows) that is parallel to

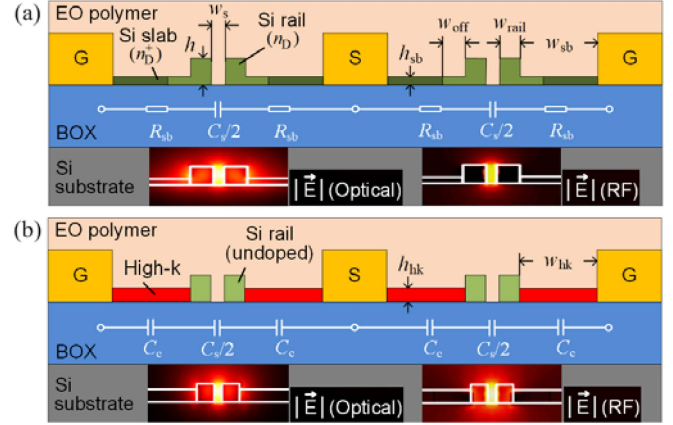


Fig. 6. Mach-Zehnder modulator cross-sections. (a) Resistively-coupled (RC) slot WG formed by two silicon (Si) rails (green) with typical heights $h = (200 \dots 400)$ nm and widths $w_{rail} = (150 \dots 240)$ nm, which are separated by a gap of width $w_s = (80 \dots 200)$ nm. A cover of organic EO material (light orange) fills also the slot. The Si rails are connected to the metal strips (height h_m) of the GSG transmission line (yellow) through doped Si slabs (green). At low frequencies, the RF modulating voltage drops predominantly across the slot region. To reduce optical loss, a smaller doping concentration n_D^- is used in the rails and in the directly adjacent slab regions of width w_{off} (light green), whereas the slab regions further away from the optical slot waveguide (dark green) are subjected to a higher doping concentration n_D^+ [48]. A simplified equivalent-circuit model is depicted as a white overlay. The slot is represented by capacitance $C_s/2$, which is connected to the ground and the signal strip of the transmission line through a total slab resistance $2R_{sb}$. The insets in the grey substrate region are the electric-field profiles of the optical quasi-TE mode and the RF mode. (b) Capacitively-coupled (CC) slot WG. The doped Si slabs in the upper panel (a) are substituted by a high- k dielectric material (red, relative permittivity $\epsilon_{r,BTO} = 18$ at microwave frequencies, refractive index $n_{BTO} = 1.85$ at optical frequencies) with width w_{hk} and height h_{hk} . As depicted in the equivalent circuit, the slot capacitance $C_s/2$ is electrically connected to the electrodes through a coupling capacitance $C_c \gg C_s$ so that the RF voltage applied to the transmission line drops predominantly across the slot. In contrast to RC-SOH modulators and with a properly chosen high- k material, CC-SOH devices do not suffer from optical loss in the Si rails and from RC time constants associated with resistive coupling. (Figures adapted from [49]).

the chromophore alignment in one MZM arm and anti-parallel in the other one, resulting in push-pull operation of the MZM. For operating the modulator in a nearly linear regime of its sinusoidal electro-optic characteristic, the device is biased with a DC voltage at the null point (for amplitude modulation), or at the 3 dB point (for intensity modulation). In Fig. 5(c), the normalized optical transmission as a function of the bias voltage is shown [11] for an $L = 1$ mm long device with a half-wave voltage $U_\pi = 0.5$ V.

In combination with the resistance of the doped Si slabs, the slot capacitance forms a first-order low-pass filter for the EO transduction process. For maximizing the RC-bandwidth while minimizing optical losses introduced by free carrier absorption in the silicon slabs and rails, a multi-level doping scheme (n_D^- , n_D^+) can be employed [11], [48] as is to be seen in Fig. 6(a).

B. SOH Modulator With Capacitively-Coupled (CC) Electrodes

As mentioned in Section IV-A and explained in more detail in Section V-A, SOH devices achieve high modulation efficiencies through a strong interaction of the optical and electric fields

within the organic EO material in the slot region. In so-called resistively-coupled SOH devices (RC-SOH) as described in the previous section, the confinement of the electric field is accomplished by resistively connecting the metal electrodes with the Si slot waveguide through doped Si slabs, forming a serial RC circuit, Fig. 6(a), that limits the bandwidth of the device. The RC time constant is determined by the resistance of the doped Si slabs and the capacitance of the slot waveguide.

To overcome this bandwidth limitation, capacitively-coupled SOH devices (CC-SOH) illustrated in Fig. 6(b) can be used [49], substituting the doped Si slabs from Fig. 6(a) by high- k dielectric slabs. This dielectric material should be chosen such that its relative permittivity at microwave frequencies is much larger than that of silicon and of the organic EO material, while it is smaller than the permittivity of silicon at optical frequencies to maintain the optical waveguiding. The use of such a high- k dielectric material results in a large coupling capacitance, thereby achieving an efficient transfer of the RF electric field to the slot region, without impairing the confinement of the optical mode. Thus, the capacitive coupling scheme used in CC-SOH devices circumvents the RC bandwidth limitation. The bandwidth of CC-SOH devices is hence only limited by the frequency-dependent propagation loss experienced by the modulating RF signal, by the RF impedance mismatch, and by the velocity mismatch between the RF and the optical waves. Since the silicon rails can be left undoped, the device can also benefit from reduced optical losses when using an appropriate high- k material.

In [49], CC-SOH devices were demonstrated using barium titanate (BaTiO_3 , BTO) as a high- k dielectric material. An electro-optic 3 dB-bandwidth of 76 GHz and a 6 dB-bandwidth of 110 GHz (power of photocurrent reduced by 4) was reported along with a small π -voltage of 1.3 V ($U_\pi L = 1.3$ Vmm), limited by the rather thin gold transmission lines used in this experiment. The functionality of the device was demonstrated by generating data signals using a four-state pulse-amplitude modulation format (PAM4) at line rates of 200 Gbit/s. The BTO slabs have a relative permittivity $\epsilon_{r,\text{BTO}} = 18$ and were in an amorphous phase. According to [50], the relative permittivity of polycrystalline BTO can exceed 100 which would lead to a better RF field confinement and therefore to an even smaller $U_\pi L$.

C. Silicon-Polymer-Hybrid (SPH) Modulator

Another variant of the SOH modulator avoiding any resistive coupling is the so-called silicon-polymer hybrid (SPH) device [51], Fig. 7. Instead of a slot waveguide, very thin (40 nm) silicon strip waveguides form an MZI, the arms of which are covered with a $1 \mu\text{m}$ thick EO polymer, acting as phase shifter sections. In this specific implementation, the field around each of these waveguides hosts 74% of the total modal cross-section power. Two independent travelling-wave electrodes on top of the PS sections propagate the RF drive field. The low dielectric constant of the EO polymer results in a comparable size of the effective refractive indices [52] for the RF field ($n_{\text{el}} = 1.52$) as well as for

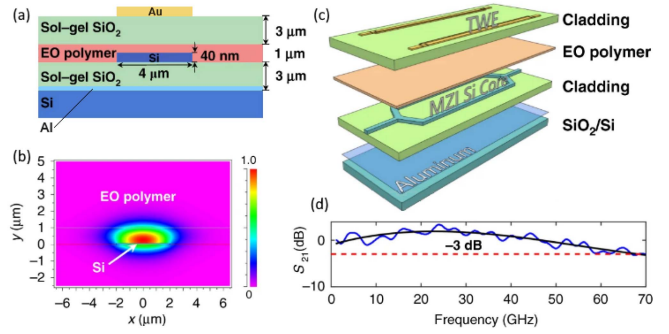


Fig. 7. Silicon-polymer hybrid (SPH) modulator for $\lambda = 1.55 \mu\text{m}$ with length $L = 8$ mm, $U_\pi L = 14.4$ Vmm, and WG loss 0.22 dB/mm. (a) Layer cross-section (b) Calculated optical field distribution around the Si core (c) Exploded perspective view of layers. From bottom: Aluminum ground plane on SiO_2/Si ; ultra-thin (40 nm) silicon; WG forming a Mach-Zehnder interferometer (MZI Si Core, arm spacing $200 \mu\text{m}$) with $1 \mu\text{m}$ thick EO polymer cover, both embedded in a sol-gel SiO_2 cladding; on top, two independent travelling-wave electrodes (TWE). (d) Measured EO transmission S_{21} in dB, 3 dB bandwidth 68 GHz. The solid black line is a fitted curve. (Figures adapted from [51]).

the lightwave [51] ($n_{\text{SPH}} = 1.66$), so that the velocity mismatch is small: This leads to a 3 dB-bandwidth of 68 GHz.

As discussed in Section II, the EO activity of the polymer can be high. From a measured in-device figure of merit of $n_{\text{SPH}}^3 r_{33} = 1021$ pm/V at $\lambda = 1.55 \mu\text{m}$ (see (12) in Section V-A) an EO coefficient of $r_{33} = 223$ pm/V can be estimated. The WG shape and an effective index of the mode close to the cladding index leads to a low propagation loss of 0.22 dB/mm. This and the ultra-high glass transition temperature $T_g = 172$ °C of the EO polymer allow operation at 110 Gbit/s OOK in a harsh environment with a wide temperature range (25...110) °C.

As a disadvantage, SPH devices offer only comparatively large half-wave voltage-length products compared to SOH devices (e.g., $U_\pi L = 14.4$ Vmm), so that large footprints result (e.g., $L = 8$ mm). In addition, the fabrication process cannot easily be integrated into a standard CMOS line. With respect to its $U_\pi L$ -product, the SPH phase shifter is comparable to CMOS-compatible carrier-depletion type *pin*-diode phase shifters, but does not suffer from a parasitic amplitude modulation.

V. PERFORMANCE AND APPLICATIONS

A. Definition of Metrics

The performance of SOH Mach-Zehnder modulators needs to be characterized by quantitative figures of merit (FOM), see the following Table I. This allows to find the optimum design for a certain application and to compare different schemes. The most important metric is the half-wave voltage-length product $U_\pi L$ (modulation efficiency). In the following paragraphs, we introduce various performance metrics, which we use to benchmark different SOH and POH MZM as well as IQ modulators that have been demonstrated over the previous years, see Section V-B, Table II.

Half-wave voltage-length product: We denote the free-space propagation constant of a monochromatic field $e^{j\omega t}$ with frequency $f = \omega/(2\pi)$ by $k_0 = \omega/c = 2\pi/\lambda$ (vacuum speed of

TABLE I
FIGURES OF MERIT (FOM). SYMBOLS AND THEIR MEANING

FOM	Definition
$U_\pi L$	Half-wave voltage-length product of the EO modulator (4)
$n_{EO}^3 r_{33}$	In-device EO figure of merit (12)
L_{eff}	Effective electrical length of EO modulator (14)
$U_\pi L a$	Half-wave voltage-loss product of the EO modulator (17)
η_{EO}	EO power conversion efficiency (19)
$f_{X,3\text{dB}}$	EO 3 dB bandwidths (22), (23), (26), (27), (28)
BVR	EO bandwidth half-wave voltage ratio (28)
$W_{\text{bit}}^{\text{TW}}$	Average energy dissipated in a load resistor during a symbol duration for NRZ-OOK modulation of an MZM with traveling-wave electrodes (29)
$W_{\text{bit}}^{\text{C}}$	Average energy dissipated in a load resistor during a symbol duration for NRZ-OOK modulation of an MZM with lumped electrodes (30)
$\frac{\Delta Q}{\Delta \Phi}$	Ratio of charge transport and phase shift between the arms of an MZM (31)
$W_{\pi,1\text{dB}}$	Energy dissipated in an MZM to produce a phase shift of π with 1 dB optical insertion loss (32)

light c , vacuum wavelength $\lambda = 1.55 \mu\text{m}$). The propagation constant β of a lossless slot-WG mode (propagator $e^{-j\beta z}$ along the z -axis pointing into the drawing plane of Fig. 6) is associated with an effective refractive index $n_e = \beta/k_0$. We assume that the modulating RF drive field $E_{d,x}(x, y) = U_d/w_s$ is spatially constant inside the slot with width w_s , and is dominantly oriented along the x -direction, i.e., horizontally in Figs. 5 and 6, so that it can be represented by the drive voltage U_d between the two silicon rails.

This is not quite true for CC electrodes and undoped rails, as can be seen from Fig. 6(b) (RF plot). Slight doping of the rails, however, leads to an increased confinement of the electrical RF field $E_{d,x}(x, y)$ within the EO material inside the slot, Fig. 6(a) (RF plot), but generally, the spatial dependencies of refractive indices and electric drive field have to be taken into account by a numerical evaluation ([49] Supplementary Material, Sect. 5).

The WG is clad and the slot is filled with an EO organic material having a refractive index n_{EO} . Exploiting the Pockels effect, an applied (possibly time-varying) drive voltage U_d changes the refractive index by Δn_{EO} , and this changes the phase of the optical quasi-TE mode. For simplicity, the refractive index change in the slot is assumed to be $\Delta n_{EO,\text{slot}}$, but zero outside. The effective index of the propagating mode varies by Δn_e , and the modal phase changes by $\Delta \Phi$ [11] after the device length L ,

$$\Delta \Phi = -k_0 \Delta n_e L,$$

$$\Delta n_e = \Gamma_{\text{slot},x} \Delta n_{EO,\text{slot}}, \quad \Delta n_{EO,\text{slot}} = -\frac{1}{2} n_{EO}^3 r_{33} \frac{U_d}{w_s}. \quad (3)$$

The quantity $\Gamma_{\text{slot},x}$ is the field interaction factor. Its subscript x reflects the assumption that electrical and optical electric field as well as the poling orientation of the EO material are in parallel and oriented along the x -axis (horizontal direction in Fig. 5 (Inset) and Fig. 6). The field interaction factor describes how the refractive index change inside the slot influences the modal propagation constant β and the effective index n_e of the

optical mode. The change $\Delta n_{EO,\text{slot}}$ of the refractive index in reaction to a field $E_{d,x}(x, y) = U_d/w_s$ is determined [62] by the dominant EO coefficient $r_{33} = -2\chi_{333}^{(2)}/n_{EO}^4$ [10] [Eq. (5)], [64] [Eq. (2.20)] of the organic material in the slot.

To achieve complete extinction (destructive interference), the phase difference in both arms must be $\Delta \varphi = \pi$. For push-pull operation the modulus of the required phase shift per arm is half this amount, $\Delta \Phi = \Delta \varphi/2 = \pi/2$. The corresponding driving half-wave voltage is $U_d = U_\pi$, and the voltage-length product becomes with (3)

$$\Delta \Phi = \frac{\Delta \varphi}{2} = \frac{\pi}{2}, \quad U_\pi L = \frac{1}{2} \frac{\lambda_0 w_s}{n_{EO}^3 r_{33}} \frac{1}{\Gamma_{\text{slot},x}}. \quad (4)$$

The smaller $U_\pi L$ is, the smaller the drive voltage U_d may be for a given phase modulation. According to (3), it is the field interaction factor $\Gamma_{\text{slot},x}$ that relates the effective modal index change Δn_e to the slot index change $\Delta n_{EO,\text{slot}}$, which is controlled by the drive voltage U_d ,

$$\Gamma_{\text{slot},x} = \frac{\Delta n_e}{\Delta n_{EO,\text{slot}}} = \frac{n_{\text{eg}}}{n_{EOg}} \Gamma, \quad \Gamma = \frac{W_{\text{slot}}}{W}. \quad (5)$$

Equation (5) implies a proportionality of the field interaction factor $\Gamma_{\text{slot},x}$ with the field confinement factor Γ that is defined by the ratio of the energy W_{slot} in the slot and the total mode energy W . The ratio n_{eg}/n_{EOg} of effective group refractive index n_{eg} of the slot-waveguide mode and group refractive index of the underlying material, $n_{EOg} = n_{EO} + \omega dn_{EO}/d\omega$, connects $\Gamma_{\text{slot},x}$ and Γ . This relation will be proved in the following.

First we apply a variation theorem for dielectric waveguides [63] [Eq. (2.2.73)]. Given a mode with cross-sectional power P , this theorem specifies a perturbation $\delta\beta$ in the propagation constant for perturbations $\delta(\omega \epsilon_0 \epsilon_r)$ and $\delta(\omega \mu_0)$,

$$\delta\beta = \frac{1}{4LP} \iiint_V \left(\delta(\omega \epsilon_0 \epsilon_r) |\vec{E}|^2 + \delta(\omega \mu_0) |\vec{H}|^2 \right) dV, \\ P = \frac{1}{2} \iint_A \Re \left\{ \vec{E} \times \vec{H}^* \right\} \cdot \vec{e}_z dx dy. \quad (6)$$

We previously assumed that the drive voltage changes the relative permittivity in the slot only, $\Delta \epsilon_r \approx 2n_{EO} \Delta n_{EO,\text{slot}}$, therefore we find with $\delta\omega = 0$ and $\Delta n_e = \Delta \beta/k_0$

$$\Delta n_e = \frac{c\epsilon_0}{2LP} \iiint_{V_{\text{slot}}} n_{EO} \Delta n_{EO,\text{slot}} |\vec{E}|^2 dV. \quad (7)$$

We further assume that n_{EO} and $\Delta n_{EO,\text{slot}}$ are spatially constant inside the slot volume $V_{\text{slot}} = A_{\text{slot}} L$ with cross-section A_{slot} and length L , and that the magnitude of the optical electric field depends on the transverse coordinates x, y only. Note however, that, for CC electrodes, this approximation is quite coarse, see the text in the paragraph preceding the one with (3). In addition, we introduce the vacuum wave impedance $Z_0 = 1/(c\epsilon_0)$. The field interaction factor then reads

$$\Gamma_{\text{slot},x} = \frac{\Delta n_e}{\Delta n_{EO,\text{slot}}} = \frac{n_{EO} \iint_{\text{slot}} |E_x(x, y)|^2 dx dy}{Z_0 \iint_A \Re \left\{ \vec{E} \times \vec{H}^* \right\} \cdot \vec{e}_z dx dy}. \quad (8)$$

The field confinement factor Γ is the ratio of the modal energy W_{slot} in the slot volume related to the modal energy W stored in

the full modal volume with cross-section A . For the time average of the field energy W [63] [Eq. (2.2.79)] we write

$$\begin{aligned} W &= \frac{1}{4} \iiint_V \left(\frac{d(\omega \varepsilon_0 \varepsilon_r)}{d\omega} |\vec{E}|^2 + \frac{d(\omega \mu_0)}{d\omega} |\vec{H}|^2 \right) dV \\ &= \frac{1}{4} \varepsilon_0 \iiint_V \left[n \left(n + 2n \omega \frac{dn}{d\omega} \right) |\vec{E}|^2 + n^2 |\vec{E}|^2 \right] dV \\ &= \frac{1}{4} \varepsilon_0 \iiint_V 2n n_g |\vec{E}|^2 dV. \end{aligned} \quad (9)$$

The derivative $d(\omega \varepsilon_r)/d\omega = \varepsilon_r + \omega d\varepsilon_r/d\omega$ implies a term which changes the electric field energy by material dispersion that is intimately connected to a dissipation of energy as formulated by the Kramers-Kronig relations. We assume a transparent medium, where in the region of interest the energy dissipation can be neglected, and in this spirit the magnetic field energy $\int \mu_0 |\vec{H}|^2 dV$ and the electric field energy $\int \varepsilon_0 \varepsilon_r |\vec{E}|^2 dV$ are approximately equal.

As before we assume that the permittivities and the respective refractive indices n , n_{EO} as well as the group quantities n_g , n_{EOg} are spatially constant in the relevant integration regions. With the help of (9) we calculate the field confinement factor

$$\Gamma = \frac{W_{\text{slot}}}{W} = \frac{1}{W} \frac{1}{4} 2n_{EO} n_{EOg} \varepsilon_0 L \iint_{\text{slot}} |\vec{E}(x, y)|^2 dx dy. \quad (10)$$

With the field energy per length W/L from (9) we find the group index of the mode either from [63] [Eq. (2.2.81)], $n_{eg}/c = W/(LP)$, or by applying the variation theorem (6) when all variations are caused by perturbations in ω alone, $n_{eg}/c = d\beta/d\omega$. We then prove with (10) and comparing to (8) the second relation for $\Gamma_{\text{slot},x}$ in (5),

$$n_{eg} = \frac{cW/L}{P}, \quad \frac{n_{eg}}{n_{EOg}} \Gamma = \frac{\frac{1}{2} n_{EO} c \varepsilon_0 \iint_{\text{slot}} |\vec{E}(x, y)|^2 dx dy}{\frac{1}{2} \iint_A \Re \left\{ \vec{E} \times \vec{H}^* \right\} \cdot \vec{e}_z dx dy}. \quad (11)$$

This finding can be physically interpreted as follows: The larger Γ is, i.e., the stronger the optical field is confined to the slot, the more efficient a voltage-driven slot index change $\Delta n_{EO, \text{slot}}$ leads to an effective modal index change Δn_e .

However, Δn_e also depends on the time it takes for the mode to propagate through the PS section: The slower the propagation is, the more effective the interaction with the nonlinear medium will be. The quantities n_{eg} and n_{EOg} are the group indices associated with n_e and n_{EO} . Their ratio n_{eg}/n_{EOg} reflects the ratio of time that the mode stays in the PS region, related to the time it would dwell if propagating in bulk electro-optic material having the same properties as that in the slot. Specifically for slow-light structures, $\Gamma_{\text{slot},x} > 1$ becomes possible.

With respect to efficiency, SOH MZM stand out due to low half-wave voltage-length products down to $U_\pi L = 0.32$ Vmm, which is approximately an order of magnitude smaller than the half-wave voltage-length products of competing modulator technologies [24]. POH devices can reduce $U_\pi L$ by another order of magnitude [45], but they suffer from significant optical losses, see discussion of the half-wave voltage-loss product $U_\pi L a$ after (17) below.

In-device EO FOM: When changing the drive voltage U_d , we record a trace like in Fig. 5(c) from which we determine the half-wave voltage U_π . We measure the slot width w_s and determine $\Gamma_{\text{slot},x}$ by a numerical simulation. Substituting the results in (4), we find $n_{EO}^3 r_{33}$ as the in-device EO figure of merit,

$$n_{EO}^3 r_{33} = \frac{1}{2} \frac{\lambda_0 w_s}{U_\pi L} \frac{1}{\Gamma_{\text{slot},x}}. \quad (12)$$

The larger $n_{EO}^3 r_{33}$ is, the smaller the drive voltage U_d may be. If a reliable estimate of the refractive index n_{EO} is available, the EO coefficient r_{33} can be determined. However, also the measurement of the effective slot with w_s and the numerical calculation of the field interaction factor $\Gamma_{\text{slot},x}$ gives rise to uncertainties.

Effective modulator length: The modulator's transmission line electrodes are lossy and attenuate the propagating electrical mode. Due to the skin effect, the RF power attenuation constant α_{RF} in (13) depends on the modulation frequency $f_m = \omega_m/(2\pi)$, $\alpha_{RF}(f_m) = \alpha_c \sqrt{f_m}$, where the factor α_c accounts for the conductor's material parameters. Neglecting impedance mismatch and walk-off, the modulation amplitude $U_m \propto \Delta\Phi$ of the drive voltage $U_d = U_m \sin(\omega_m t)$ controls the phase shift $\Delta\Phi$ of (3) and decays with $U_m(z) = U_m(0) e^{-\alpha_{RF}(f_m) z/2}$. The phase shift along a modulator length L results by integrating the local voltage-proportional phase shifts [64] [Eq. 2.42)],

$$\Delta\Phi(f_m) = \Delta\Phi_0 \frac{1}{L} \int_0^L e^{-\frac{1}{2} \alpha_{RF}(f_m) z} dz = \Delta\Phi_0 \frac{L_{\text{eff}}(f_m)}{L}. \quad (13)$$

This defines a frequency-dependent effective electrical length $L_{\text{eff}} < L$ (if $\alpha_{RF} \rightarrow 0$, then $L_{\text{eff}} \rightarrow L$),

$$L_{\text{eff}}(f_m) = \frac{2}{\alpha_{RF}(f_m)} \left(1 - e^{-\frac{1}{2} \alpha_{RF}(f_m) L} \right). \quad (14)$$

The frequency $f_m = f_{L \text{ 3dB}}$ where $L_{\text{eff}}(f_m) = L/\sqrt{2}$ holds, determines the loss-dependent roll-off frequency

$$f_{L \text{ 3dB}} = 0.54/(\alpha_c L)^2. \quad (15)$$

Half-wave voltage-loss product: The optical MZM input power P_{opt} is split evenly between the two MZM arms by an MMI as in Fig. 5(b). At the MZM output there is another MMI which adds the fields of both arms. If the modulator is biased at its 3 dB point, only half of the input power would leave the output port of the modulator's output MMI, if it was not for the optical power loss in the MZM arms. The associated optical power attenuation constant α_0 (unit 1/mm) can be regarded to be constant near the optical operating frequency f_0 . For the MZM output power P_o and for the length-related optical insertion loss a (measured in dB/mm) we find

$$\begin{aligned} P_o &= \frac{1}{2} P_{\text{opt}} e^{-\alpha_0 L} \quad (3 \text{ dB-bias}, \Delta\varphi_{3\text{dB}} = \pi/2), \\ a &= \frac{1}{L} 10 \log_{10} (e^{\alpha_0 L}) = 4.34 \alpha_0. \end{aligned} \quad (16)$$

The optical insertion loss $L a$ (measured in dB) depends on the device length L of the MZM. Doping the slabs and rails is a major source of optical loss, and sidewall roughness of the

slot WG contributes, too. For resistively coupled modulators, $a = 2.5$ dB/mm was measured [23], but roughness-determined optical insertion losses below $a = 1$ dB/mm are expected [49]. To account for the modulator loss, the U_π -loss product $U_\pi L a$ (measured in V dB) is defined [11],

$$U_\pi L a = \frac{1}{2} \frac{\lambda_0 w_s}{n_{\text{EO}}^3 r_{33}} \frac{1}{\Gamma_{\text{slot},x}} a. \quad (17)$$

The smaller the U_π -loss product $U_\pi L a$ is, the better is the device. The metric of x V dB describes the half-wave voltage $U_\pi = x$ V for an MZM with optical insertion loss $La = 1$ dB, or alternatively, it specifies the insertion loss $La = x$ dB of a device with a half-wave voltage $U_\pi = 1$ V.

With respect to $U_\pi L a$, SOH modulators can reach values down to 1.0 V dB [23], which is among the lowest values so far demonstrated irrespective of modulator technology. In contrast to that, POH devices suffer from significant optical loss, leading to $U_\pi L a$ -products in excess of 10 V dB, despite their low $U_\pi L$.

Electro-optic conversion efficiency: Radio-over-fiber (RoF) denotes a technology where radio frequency (RF) signals are transmitted over optical fibers by modulating an optical carrier. Technical advantages of this transmission method as compared to RF cables are the immunity with respect to RF interference and noise, the large bandwidth and the low transmission loss, and the compactness of the fiber. These advantages are also of interest for RF read-out of cryogenic electrical circuits, but it is especially the low thermal conductivity of glass fibers which makes the technology attractive for this application, see Section V-C.

In the context of these applications, an important metric is the electro-optic conversion efficiency η_{EO} of the electro-optic modulator. The basic setting of an RoF transmitter is as follows: An optical field with effective input power P_{opt} feeds an MZM. The travelling wave electrodes of the MZM have a real line impedance Z_L and are terminated with a matched resistor. The modulator is biased at its 3 dB point, in which the phase difference of the signals coming from the two MZM arms amounts to $\Delta\varphi_{3\text{dB}} = \pi/2$, for intensity modulation with best efficiency. An RF voltage $U_d = U_m \sin(\omega_m t)$, where both, U_m and ω_m , could depend on time, drives the electrodes with an RF power $P_d = U_m^2/(2Z_L)$, $U_m \leq U_\pi$, and modulates the phase difference $\Delta\Phi_{\text{MZM}}(t)$ of both arms with a phase modulation index $\eta_m \leq \pi/2$ according to

$$\begin{aligned} \Delta\Phi_{\text{MZM}}(t) &= \Delta\varphi_{3\text{dB}} + \varphi(t), \\ \varphi(t) &= \eta_m \sin(\omega_m t), \quad \eta_m = \frac{\pi U_m}{2 U_\pi}. \end{aligned} \quad (18)$$

Consequently, the optical fields in both arms become phase-modulated, which leads to a spectrum described by Bessel functions [65]. In the small-signal case, i.e., for modulation indices $\eta_m \ll 1$, the zeroth-order and the first-order Bessel functions for carrier and sideband can be approximated by $J_0(\eta_m) = 1$ and $J_1(\eta_m) = \eta_m/2$, respectively, while higher-order sidebands may be safely neglected. The relative phase differences of the first sidebands at frequencies $f_0 \pm f_m$ with respect to the carrier at frequency f_0 are the same as for amplitude modulation. The optical carrier power at the MZM output amounts to

$P_0 = J_0^2(\eta_m)P_{\text{opt}}/2$, and the power of each of the two first-order modulation sidebands is $P_1 = J_1^2(\eta_m)P_{\text{opt}}/2$. The electro-optic power conversion efficiency in the small-signal case then reads

$$\eta_{\text{EO}} = \frac{P_1}{P_d} = \frac{(\eta_m/2)^2 P_{\text{opt}}/2}{U_m^2/(2Z_L)} = \frac{\pi^2 Z_L P_{\text{opt}}}{16 U_\pi^2}, \quad \eta_m \ll 1. \quad (19)$$

The signal $U_d = U_m \sin(\omega_m t)$, upconverted to the first order optical sidebands, can be downconverted by detecting the strong carrier and the small sidebands with a photodetector in the next step. The photodetector output current contains a mixing term of carrier and sideband fields, $\sqrt{P_0} \cos(\omega_0 t) \times \sqrt{P_1} \cos[(\omega_0 \pm \omega_m)t]$, which oscillates with the modulation frequency ω_m and which has an amplitude proportional to U_m . Using (19) we find the photocurrent

$$i_m \propto \sqrt{P_0} \sqrt{\eta_{\text{EO}} P_d} \cos(\omega_m t) \propto \sqrt{\eta_{\text{EO}}} U_m \cos(\omega_m t). \quad (20)$$

Obviously, $\sqrt{\eta_{\text{EO}}}$ acts as an amplification factor for a linear voltage ‘‘amplifier’’. The conversion efficiency η_{EO} can be improved either by increasing the effective optical input power P_{opt} of the modulator, or by decreasing its half-wave voltage U_π .

However, if U_π should become smaller, the modulator must become longer for a given design, (4). As a consequence, the loss increases, and the optical power P_{opt} in (19) decreases exponentially, $P_{\text{opt}} e^{-\alpha_0 L}$, see (16). To find the optimum length which yields maximum conversion efficiency, we multiply numerator and denominator in (19) with L^2 and use the fact that the product $U_\pi L$ is a constant related to the modulator technology. The conversion efficiency η_{EO} is then maximized for an optimum length $L = 2/\alpha_0$,

$$\begin{aligned} \eta_{\text{EO,max}} &= \frac{P_1}{P_d} \Big|_{\text{max}} = \frac{\pi^2 Z_L P_{\text{opt}}}{16 \underbrace{(U_\pi L)^2}_{\text{const}}} \underbrace{L^2 e^{-\alpha_0 L}}_{\text{max: } (2/(\alpha_0 e))^2 \text{ for } L=2/\alpha_0} \\ &= \frac{\pi^2}{4e^2} \frac{Z_L P_{\text{opt}}}{(U_\pi L \alpha_0)^2} = 6.29 \frac{Z_L P_{\text{opt}}}{(U_\pi L a)^2}. \end{aligned} \quad (21)$$

With (17) we find that a small half-wave voltage-loss product $U_\pi L a$ (measured in V dB) leads to a large maximum electro-optic conversion efficiency $\eta_{\text{EO,max}}$.

EO bandwidth: The electro-optic bandwidth of a modulator is an important characteristic. A full description including also walk-off can be found in [69], [70], [71]. To separate the effects and to simplify the derivations, optical loss and a possible mismatch between electrical phase velocity v_{el} and optical group velocity v_{g} resulting in a walk-off are considered independently in the following.

The MZM bandwidth is essentially determined by the electrical equivalent circuits which drive the phase modulator sections. Fig. 8(a) represents the travelling-wave transmission line by a differential electrical equivalent circuit which is resistively-coupled (RC) to the optical slot WG. Fig. 8(b) stands for a differential element of a capacitively coupled (CC) electrical transmission line. Both circuits contain resistive elements which attenuate the propagating electrical amplitude according to the frequency-dependent power attenuation constant $\alpha_{\text{RF}}(f_m)$ (unit 1/mm), (14).

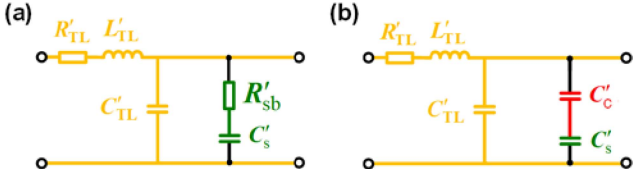


Fig. 8. Differential electrical circuits of travelling-wave modulators. The quantities $X'_{TL, sb, hk, s} = dX_{TL, sb, hk, s}/dz$ represent differential circuit elements of a differential coplanar transmission line section with length dz (R'_{sb} has to be interpreted as $1/R'_{sb} = G'_{sb} = d(1/R_{sb})/dz = dG_{sb}/dz$). **Yellow elements** belong to the metallic electrodes. (a) Resistively-coupled (RC) transmission line. **Green elements** represent the RC shunt load formed by the doped Si slab R'_{sb} and the Si slot capacitance C'_s . (b) Capacitively-coupled (CC) transmission line. **Red and green elements** stand for the shunt load formed by the series connection of the high-k dielectric coupling slab C'_c and the slot capacitance C'_s , respectively. (Figures adapted from [66]).

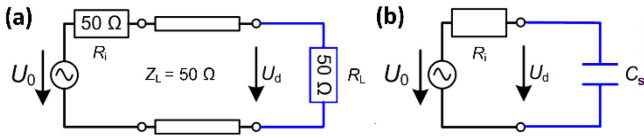


Fig. 9. Equivalent electrical circuits of modulators. (a) Travelling-wave electrodes form a transmission line with line impedance $Z_L = 50 \Omega$, matched to generator and terminating resistor. The drive voltage along the transmission line is $U_d = U_0/2$. (b) Lumped element electrodes represented by the slot capacitance C_s . Compared to the matched transmission line, the drive voltage is doubled, $U_d = U_0$. (Figures adapted from [11]).

For a push-pull MZM, the phase difference between the fields in the two arms amounts to $\Delta\Phi_{MZM} \propto U_d$. The drive voltage U_d depends on the generator voltage U_0 in Fig. 9(a) through an electrical network with transfer function $\tilde{h}(f_m)$. In the following, we interpret the “zero” modulation frequency “ $f_{m,0} = 0$ ” as a frequency $f_{m,0} \ll f_{3dB}$. We then find the electro-optic transfer function $m_{EO}(f_m)$ of an MZM with length L [66] [Eq. (2.31)] and the associated 3 dB bandwidth f_{3dB} ,

$$m_{EO}(f_m) = \frac{\Delta\Phi_{MZM}(f_m)}{\Delta\Phi_{MZM}(0)} = \tilde{h}(f_m)L_{\text{eff}}(f_m)/L,$$

$$|m_{EO}(f_{3dB})| = |m_{EO}(0)|/\sqrt{2}, \quad f_{L\ 3dB} = 0.54/(\alpha_c L)^2. \quad (22)$$

The RF loss-limited frequency $f_{L\ 3dB}$ was derived in (15). The conversion efficiency (19) depends on η_{im}^2 , which is in proportion to $\Delta\Phi_{MZM}^2$ according to (18). Therefore the 3 dB limiting frequency f_{3dB} from (22) determines the limiting frequency for η_{EO} ,

$$\eta_{EO}(f_m) = |m_{EO}(f_m)|^2 \eta_{EO}(0), \quad \eta_{EO}(f_{3dB}) = \eta_{EO}(0)/2. \quad (23)$$

If RF losses can be neglected, the electrical transfer functions $\tilde{h}(f_m) = \{\tilde{h}_{RC}(f_m), \tilde{h}_{CC}(f_m)\}$ for RC and CC-coupled modulators can be approximately determined by a voltage divider relation, i.e., by the fraction of the transmission line drive voltage which drops across the differential slot capacitance C'_s [66] [Eq.

(2.31),(2.32)],

$$\tilde{h}_{RC}(f_m) = \frac{1}{1 + j\omega_m R'_{sb} C'_s}, \quad \tilde{h}_{CC}(f_m) = \frac{1}{1 + C'_s/C'_c} \stackrel{C'_c \gg C'_s}{\approx} 1. \quad (24)$$

From (24) we see that the CC-SOH modulator has a frequency-independent transfer function $\tilde{h}_{CC}(f_m)$ and thus overcomes the $R'_{sb}C'_s$ bandwidth limitation of the conventional resistively-coupled SOH devices. However, if the condition $C'_c \gg C'_s$ cannot be met, the effective drive voltage across C'_s is reduced.

If the transmission line is electrically short compared to the smallest RF wavelength of interest and therefore needs no termination as in Fig. 9(b), the electro-optic transfer function is determined by the internal resistance $R_i = 50 \Omega$ of the modulation source, and by the lumped slot capacitance C_s . In the specific case [64] [Page 151], the slab resistance $R_{sb} \approx 18 \Omega$ is about three times smaller than R_i , so it is disregarded in this estimate,

$$m_{EO}^{\text{imp}}(f_m) = \frac{\Delta\Phi_{MZM}^{\text{imp}}(f_m)}{\Delta\Phi_{MZM}^{\text{imp}}(0)} = \tilde{h}_{R_i C_s}^{\text{imp}} = \frac{1}{1 + j\omega_m R_i C_s}. \quad (25)$$

The frequency, where the moduli of the electro-optic transfer functions (24), (25) drop by a factor $1/\sqrt{2}$, is called the limiting RC frequency,

$$f_{RC\ 3dB} = \frac{1}{2\pi R'_{sb} C'_s}, \quad f_{RC\ 3dB}^{\text{imp}} = \frac{1}{2\pi R_i C_s}. \quad (26)$$

The prominent advantage of an electrically short MZM is the doubling of the drive voltage compared to the travelling-wave case, but because usually $R_i = 50 \Omega$ and $R_i C_s > R'_{sb} C'_s$, this comes at the price of a reduced bandwidth.

We now assume that the transmission line is impedance-matched and terminated, and that its transmission loss is low, $L_{\text{eff}}(f_m) \approx L$ in (14). We further postulate that the electro-optic transfer function (22) is $m_{EO}(f_m) \approx 1$. If then the group velocity $v_{g,el}(f_m)$ (group delay $t_{g,el} = L/v_{g,el}$) of the electrical drive signal (which is not necessarily a sinusoidal) deviates from the optical group velocity v_g (optical group delay $t_g = L/v_g$ at the optical carrier frequency), this group delay walk-off limits the bandwidth. When electrical and optical signal envelopes have acquired a phase difference π , the walk-off limited modulation frequency for a travelling-wave modulator with length L is reached,

$$\omega_{TW\ 3dB} |t_g - t_{g,el}| = \pi, \quad f_{TW\ 3dB} = \frac{1}{2} \frac{v_g}{L} \frac{1}{|1 - v_g/v_{g,el}|}. \quad (27)$$

A more accurate analysis replaces the factor $1/2 = 0.5$ by 0.556 [9] [Eq. (3)], [67] [Eq. (A.86)], [68] [Eq. (6.28)]. Referring to optical and electrical effective phase velocities, $v_g \rightarrow v_e$ and $v_{g,el} \rightarrow v_{e,el}$, [71] [Eq. (2)] replaces the factor $1/2 = 0.5$ by 0.445 using a slightly different cut-off frequency definition. In all cases, bandwidth and length can be traded.

Measuring the total EO bandwidth $f_{\text{tot}\ 3dB}$: In small-signal approximation, the intensity change at the MZM output near the 3 dB-point is in proportion to the phase difference $\Delta\Phi_{MZM}$, which in turn is in proportion to the drive voltage $U_d(f_m)$.

The output intensity is measured with a photodiode which delivers a photocurrent with a modulation of amplitude $i_m = u_m/50 \Omega$ (voltage u_m) at frequency f_m . The element $S_{21}(f_m)$ of the scattering matrix, $S_{21}(f_m) \propto u_m(f_m)/U_d(f_m)$, can be recorded with an electrical network analyzer. The 3 dB drop of $S_{21,\text{dB}}(f_m) = 20\log_{10}(S_{21}(f_m)/S_{21}(0))$ marks the total EO bandwidth $f_{\text{tot},3\text{dB}}$ including all bandlimiting effects.

Bandwidth half-wave voltage ratio (BVR): For comparing the EO activity of different devices, the EO bandwidth half-wave-voltage ratio (BVR) is defined [51],

$$\text{BVR} = f_{\text{tot},3\text{dB}}/U_\pi, \quad \text{BVR}_{\text{TW}} = \frac{1}{2} \frac{1}{U_\pi L} \frac{v_g}{|1 - v_g/v_{g,\text{el}}|}. \quad (28)$$

The BVR is a FOM which is large for a high EO activity and indicates a high-speed operating capability. The bandwidth half-wave-voltage ratio BVR_{TW} is especially useful if $f_{\text{tot},3\text{dB}} = f_{\text{TW}3\text{dB}}$, i.e., if the bandwidth is limited by walk-off, (27). In this case, both the bandwidth and the half-wave voltage U_π decrease in proportion to the length, such that the ratio of the two quantities is constant.

Energy efficiency: Mach-Zehnder modulators have either travelling-wave or lumped electrodes, Fig. 9. We first model the electric circuit of a travelling-wave modulator as in Fig. 9(a) by a lossless transmission line, terminated on both sides with the line impedance Z_L , $R_i = Z_L = R_L$. Then the modulator drive voltage amounts to half the generator open circuit voltage, $U_d = U_0/2$. Assuming a mean-free drive signal switched between $+U_d/2$ and $-U_d/2$ for a non-return-to-zero (NRZ) on-off keying (OOK) format, the average energy $W_{\text{bit}}^{\text{TW}}$ dissipated in R_L during a symbol duration T_s is

$$W_{\text{bit}}^{\text{TW}} = T_s (U_d/2)^2 / R_L. \quad (29)$$

This relatively high amount of energy can be much reduced if the voltage-length product $U_\pi L$ is small so that the modulator length can be shortened without increasing U_π unduly, and the transmission line is reduced to a lumped capacitor. In this case the driver electronics needs to be placed close to the phase modulator sections. Then the electro-optic transfer function is given by $h_{R_i C_s}^{\text{imp}}(f_m)$ in (25).

A single charging process of the slot capacitance C_s from drive voltage $-U_d/2$ to $+U_d/2$ stores the same energy $W_s = C_s U_d^2/2$ in the capacitor (charge $Q_s = C_s U_d$) as is dissipated in the charging resistor, independent of its value. If the symbol duration is larger than the $R_i C_s$ time constant, $T_s > R_i C_s$, then the slot capacitance becomes fully charged respectively discharged during the symbol duration. For NRZ modulation, charging or discharging occurs on average only every second bit, so the dissipated energy and the average charge per bit become

$$W_{\text{bit}}^{\text{C}} = C_s (U_d/2)^2 = Q_{\text{bit}} U_d/2, \quad Q_{\text{bit}} = C_s U_d/2. \quad (30)$$

Ratio of charge transport and phase shift: The charge transport associated with a phase shift of $\Delta\Phi = \pi$ between the arms of an MZM is $\Delta Q = C_s U_\pi$ ($C_s \approx \epsilon_0 \epsilon_r h L/w_s$ as a coarse

approximation). The ratio

$$\frac{\Delta Q}{\Delta\Phi} = \frac{C_s U_\pi}{\pi} = \frac{C_s}{\pi} \frac{\lambda_0 w_s}{2n_{\text{EO}}^3 r_{33}} \frac{1}{\Gamma_{\text{slot},x} L} = \frac{\lambda_0 \epsilon_0 \epsilon_r h}{2\pi n_{\text{EO}}^3 r_{33} \Gamma_{\text{slot},x}} \quad (31)$$

does not depend on slot length L and slot width w_s . The slot height h and width are defined in Fig. 6(a).

Energy dissipated in MZM for phase shift π and 1 dB loss: The device length is related to the optical insertion loss. We compare the dissipated energy with a reference MZM having an optical insertion loss $(La)_{\text{ref}} = 1$ dB, (17). A device with insertion loss La requires a drive voltage $U_d = U_\pi(La)/1$ dB for a phase shift of π . We find the energy dissipation $W = \frac{1}{2} Q_s U_d$ for a charge transport $Q_s = \pi \Delta Q / \Delta\Phi$ as specified in (31) leading to a phase shift π in a device with 1 dB optical insertion loss [11],

$$W_{\pi,1\text{dB}} = \frac{1}{2} Q_s U_d = \frac{1}{2} \pi \frac{\Delta Q}{\Delta\Phi} U_\pi \frac{La}{1 \text{ dB}}. \quad (32)$$

From [11] [Table I] it can be seen that SOH modulators are more efficient in this respect ($W_{\pi,1\text{dB}}^{\text{SOH}} = 25$ fJ) than pn -depletion modulators ($W_{\pi,1\text{dB}}^{pn\text{-dpl}} = 5$ nJ), while POH modulators ($W_{\pi,1\text{dB}}^{\text{POH}} = 60$ fJ) are a match much closer to the SOH types.

B. Application in Communications and Sensing

Fueled by the demands of bandwidth-hungry applications such as cloud-based services, video streaming, and artificial intelligence, the growth in data traffic imposes higher capacity requirements on optical communication systems. Optical modulators are necessary for modulating electrical baseband signals on optical carriers. They are key elements in such optical communication systems and are hence in the focus of research and development activities worldwide, driven, e.g., by the migration of data center communication to 400 Gbit/s Ethernet (400 GbE) standards as well as by the growing focus on upcoming 800 GbE and 1.6 TbE with interface rates of 800 Gbit/s and 1.6 Tbit/s, respectively [72]. Importantly, high-performance EO modulators must therefore have high bandwidths while concurrently operating at low drive voltages, thereby reducing power dissipation of the device itself and of the associated drive circuitry. For cost efficiency, CMOS process compatibility and a small modulator footprint are also highly desirable. In these regards, SOH modulators have been shown to be promising candidates that can outperform most competing platforms.

There have been numerous publications demonstrating the high-speed data transmission capabilities of different SOH modulators. Amplitude modulation techniques, such as on-off-keying (OOK) and four-level pulse amplitude modulation (PAM4), have been shown using SOH MZM, while quadrature modulation techniques, such as 16-state quadrature amplitude modulation (16QAM) and quadrature phase shift keying (QPSK) have been demonstrated with in-phase/quadrature (IQ) modulators. In recent publications, the lifetime concerns of these modulators have also been addressed through long-term thermal stability testing and through the use of organic EO materials with a high glass transition temperature T_g , see Section II-C.

TABLE II
SUMMARY OF PERFORMANCE METRICS OF SOH MACH-ZEHNDER AND IQ MODULATORS

Device	Line rate [Gbit/s] (Overhead)	Modulation scheme	Drive voltage [V _{pp}]	$U_{\pi}L$ [Vmm]	Device length L [mm]	a [dB/mm]	$U_{\pi}La$ [VdB]	EO material	T_g [°C]	Ref.
Slot-WG IQ-M	400 (20%)	16QAM	1.5	1	0.6	-	-	SEO250	130 [73]	[74]
Slot-WG MZM	280 (20%)	PAM4	0.86	0.46	0.75	-	-	Perkinamine™ Series 5A	>175	[32]
	150 (7%)	OOK	0.82							
Strip-WG MZM	200 (-)	PAM4	-	14.4	8	0.22	3.2	Synthesized based on [33]	172	[51] [75]
	110 (-)	OOK								
Strip-WG MZM	110 (-)	PAM4	1.6	22	-	0.22	3.6	EO194	185	[76]
Slot-WG IQ-M	52 (7%)	16QAM	0.41	0.8	1.5	-	-	SEO100	140 [74]	[77]
Slot-WG MZM	40 (-)	OOK	0.14	0.32	1.5	9.3	7.4	JRD1	82	[24]
Strip-WG MZM (Si/InP hybrid)	252 (-)	PAM4	-	-	1.5	3.9	-	Synthesized based on [33]	172	[78]
Slot-WG CC-SOH MZM	200 (20%)	PAM4	1	1.3	1	-	-	YLD124	81 [24]	[49]
POH IQ-M	560 (27%)	16QAM	3	0.12	0.015	> 100	> 10	-	-	[79]
POH MZM	432 (16%)	PAM8	2.8	0.162	0.015	> 100	> 10	HLD1:HLD2	-	[80]

Record performance metrics for SOH devices indicated in bold.

Table II provides an overview of metrics that were experimentally demonstrated using SOH MZM and IQ modulators in recent years. It compares notable line rates, modulation schemes, and drive voltages used in various data transmission experiments. For better comparability, the relative data rate overhead required for error correction is included in the table if it was provided in the respective reference. Table II also shows some of the most important device parameters, namely the half-wave voltage-length product $U_{\pi}L$ (4), the device length L , the optical insertion loss a per length for the modulator section, (16), as well as the combined half-wave voltage-loss product $U_{\pi}La$ of (17). Furthermore, we list the used EO material and its glass transition temperature T_g . Record performance values for SOH devices in each column are in bold print. All table entries are measured for 1550 nm wavelength operation, unless otherwise indicated.

As can be seen from Table II, Wolf et al. [74] demonstrated with an SOH IQ modulator a line rate of 400 Gbit/s using a 16QAM format, the highest line rate published so far using an SOH modulator. The modulator is a slot waveguide of RC-SOH type. With a similar device architecture and amplitude modulation schemes, Eschenbaum et al. [32] showed record-high line rates of 280 Gbit/s and 150 Gbit/s with PAM4 and OOK signaling, respectively, using sub-1 V peak-to-peak drive voltages. Notably, the thermally-stable organic EO material (Perkinamine™ Series 5A, Lightwave Logic, Englewood, Colorado) used in [32] features a glass transition temperature of more than 175 °C. The modulator did not show a relevant performance degradation after thermal stress at 85 °C for 900 h.

Kieninger et al. [24] demonstrated ultra-high EO activity in an RC SOH MZM with a half-wave voltage product of $U_{\pi}L = 0.32$ Vmm. With a record low peak-to-peak drive voltage of 140 mV, OOK data transmission up to a line rate of 40 Gbit/s has been shown for a 1.5 mm long device. Exploiting the efficiency of SOH technology, amplifier-less generation and transmission

of 16QAM signals with a line rate of 52 Gbit/s was demonstrated, relying on sub-500 mV drive signals generated by a CMOS field-programmable gate array (FPGA) [77].

Weimann et al. used SOH electro-optic modulators for generation of optical frequency combs that served as multi-wavelength light source for wavelength-division multiplexing (WDM) transmission at Tbit/s data rates [120]. The device offered line spacings of up to 40 GHz and flat-top comb spectra with less than 2 dB power variations over up to 7 lines.

A variant of an SOH Mach-Zehnder modulator, based on a strip waveguide and also referred to as SPH modulator (Section IV-C, Fig. 7), was shown to achieve high PAM4 line rates of 200 Gbit/s, albeit with $U_{\pi}L$ -products about an order of magnitude larger than their SOH counterparts [51], [75]. Thanks to the device concept, the optical loss is very low and dominated by the material absorption, rendering a record-low half-wave voltage-loss product of 3.2 VdB. The thermal behavior of the SPH modulator [75] was also tested, showing stable operation up to 110 °C. SPH devices have also been operated with other ultra-high T_g materials, such as that in [52], where a 110 Gbit/s OOK line rate was achieved in combination with an EO material having $T_g = 185$ °C.

Other hybrid approaches perform remarkably well, too. Exploiting the CC-SOH concept by integration of BTO slabs into an SOH device, Ummethala et al. [49] achieved a broadband modulator and showed line rates of 200 Gbit/s with PAM4 signaling, mainly limited by the quality of the electronic drive generator. Fujikata et al. [78] have shown broadband operation of EO polymer / Si hybrid (SPH) and EO polymer / InP hybrid (IPH) optical modulators with 252 Gbit/s PAM4 signaling.

Although POH modulators are beyond the scope of this review, record values for POH devices are listed as a benchmark at the bottom of Table II. POH modulators feature a large field interaction between the optical and the electrical field and are hence highly efficient and compact. In addition, the metal pads forming

the associated plasmonic slot waveguides are highly conductive and the device capacitance is small, which leads to high bandwidths up to 500 GHz [44], [81]. On the other hand, POH modulators suffer from high optical insertion losses of typically about $\alpha = 500$ dB/mm [81]. Mardoyan et al. [79] demonstrated a line rate of 560 Gbit/s with a POH IQ-modulator and 16QAM signaling. With amplitude modulation (PAM8) in a single POH MZM, line rates up to 432 Gbit/s have been shown [80].

In addition to their key role in optical communications, modulators based on organic EO materials have emerged as versatile components with diverse applications in the fields of sensing and metrology, as has been shown in numerous scientific publications. In [82], [83], phase shifters with organic EO materials have been employed in optical phased arrays (OPAs) for ultrafast, low-power beam steering. Avoiding any moving parts, OPAs consist of a series of light-emitting apertures, each coupled to a phase shifter. The beam is steered by individually controlling the phase of the light emitted by each element, such that the resulting interference patterns in the far field occurs in the desired direction. An eight-channel OPA, shown in [83], achieved high-speed optical beam steering at a frequency of 2 MHz and boasted a total power consumption of 0.38 mW at a scanning speed of 500 kHz. Enabled by SOH modulators, OPA can achieve fast, robust, low-power and compact beam steering, making them attractive for a variety of applications, including light detection and ranging (LiDAR), network switches and optical sensors.

Lauermaun et al. [84] demonstrated a waveguide-based frequency shifter using single-sideband phase modulation. The scheme was based on an SOH slot-waveguide IQ modulator and achieved a frequency shift of up to 10 GHz and a carrier suppression of 37 dB in the small-signal regime. Frequency shifters based on SOH technologies are attractive for their compatibility with very large-scale integration (VLSI), and for their high performance, which outmatches their all-silicon serrodyne counterparts.

Recent works from Li et al. [85], [86], [87] have proposed a flexible polymer-based EO MZM to convert human electrocardiogram (ECG) signals into optical signals, with the aim of improving the fidelity of wearable medical monitoring sensors. In [85], an MZM was realized on a polydimethyl-siloxane (PDMS) substrate, covered with the crosslinked polymer Disperse Red 1 (DR1) / SU-8. Although the EO coefficient for DR1 / SU8 was only 18.3 pm/V, the modulator was able to recover ECG signals with amplitudes in the range (1..5) mV.

In [88], a proof-of-concept experiment was reported using a 100 GBd SPH silicon slot MZM, demonstrating a high-speed accelerator for an optical convolutional neural network. The accelerator scheme was used for image convolution. Having learned a test dataset, the subsequent image restoration by the neural network demonstrated a speed of 0.72 TOPS (tera operations per second). This opens new avenues for applying EO polymer modulators in machine learning applications.

There have also been a number of publications showing terahertz-to-optical conversion enabled by antenna-coupled EO polymer modulators [89], [90], [91]. Chung et al. [73] demonstrate an RF sensor based on an EO polymer-filled silicon slot

photonic-crystal waveguide (PCW) coupled to a bowtie antenna. Impinging free-space RF waves are collected by the bowtie antenna and coupled into two slotted PCW, which form an MZI. The MZI is operated in a push-pull configuration and modulates the free-space RF signal on an optical carrier. The scheme achieves a minimum detectable electromagnetic power density of 2.05 mW/m² at a frequency of 8.4 GHz. Exploiting the outstanding bandwidth of POH devices, Ummethala demonstrated conversion of a wireless communication signal at a carrier frequency of approximately 300 GHz to an optical carrier along with subsequent transmission through a fiber and coherent reception [44].

While the majority of optical modulators are operated at near-infrared wavelengths, efficient visible-light EO polymer modulators are advantageous for a many applications, including bio-sensing and optogenetics. Such a visible-light modulator was realized and demonstrated in [92] using an SPH MZM modulator with a transparent bottom electrode and an EO polymer with low absorbance for visible wavelengths. The modulator achieved a $U_{\pi}L$ of 5.2 Vmm and had low optical absorption losses of 2.6 dB/cm at an operating wavelength of 640 nm.

C. Application in Cryoelectronics

Computation and sensing concepts based on cryogenic electronics are set to usher in a paradigm shift, complementing or replacing current technologies for room temperature (RT) operation. In particular, superconducting electronics that operates below 4 K offers a range of advantages that make it attractive for various applications. For example, rapid single-flux-quantum (RSFQ) electronics operates at clock frequencies in the THz range with ultra-low switching energy, making the devices ideal for super-computing and quantum computing [53]. Nowadays superconducting quantum bits (qubits) are at the forefront [54], and RSFQ technology is a perfect readout and manipulation interface for these qubit realizations, providing a potential pathway to building scalable and fault-tolerant superconducting quantum processors. Furthermore, large arrays of ultra-sensitive and low-noise superconducting sensors, such as superconducting quantum interference devices (SQUID), transition-edge sensors (TES), microwave kinetic inductance detectors (MKID), or superconducting nanowire single-photon detectors [55], [56], [57], [58] are indispensable in a wide range of applications, including medical imaging, fundamental research, quantum technology, astronomy, and LiDAR.

One significant challenge that needs to be addressed for scaling practical use of cryogenic circuits is the implementation of efficient readout and control lines, which connect to back-end equipment operated at room temperature. Current systems use coaxial RF cables for such connections. However, these RF cables conduct heat into the cryostat, which becomes more severe as the complexity of the superconducting circuits and the number of required RF cables increases. Moreover, blackbody radiation at RT contaminates the RF lines with thermal photons, which is not desired for superconducting quantum circuits, since thermal noise limits the RF transfer of quantum states as well as an entanglement distribution between remote quantum nodes.

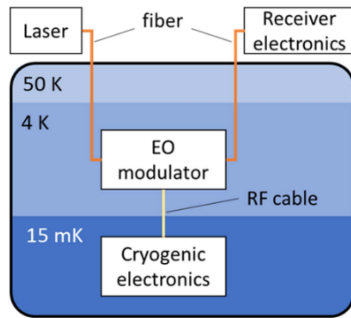


Fig. 10. Concept of a cryogenic optical egress link. The cryogenic electronics operates at temperatures down to 15 mK. An RF cable connects them to the EO modulator at the 4 K stage. Light is coupled from a laser operating at RT through a fiber into the cryostat and into the EO modulator. Another fiber connects the EO modulator to receiver electronics operating at RT.

This quantum-state transfer, however, would be needed for a number of useful quantum applications [59], [60].

One promising approach to minimize the thermal load is to use optical fibers instead of metallic readout and control lines. The thermal load introduced by an optical fiber is two orders of magnitude lower compared to a coaxial RF cable [61]. Furthermore, the high bandwidth provided by a fiber allows the multiplexing of several signals on a single fiber.

The key component for such an optical egress link is the electro-optic modulator, converting the electrical signal generated by cryogenic electronic circuits to an optical signal. The concept for this egress link is depicted in Fig. 10. The cryogenic electronics operates at a temperature of 15 mK, which is maintained by a dilution refrigerator. The EO modulator resides either in the 4 K or in the 15 mK stage of the cryostat, and is connected to the cryogenic electronics via RF cables. The optical carrier is provided by a laser operating at RT, and a fiber guides the laser light to the EO modulator.

In recent years, several electro-optic modulators have been demonstrated at cryogenic temperatures. Non-resonant schemes include a commercial lithium niobate phase shifter [61], a POH MZM [93], and a silicon MZM based on the third-order nonlinear susceptibility $\chi^{(3)}$, i.e., on the electro-optic DC Kerr effect [94].

Resonant cryogenic modulators based on ring or racetracks modulators reported to date use the materials indium phosphide [95], barium titanate [96], silicon [97], [98], or graphene [54], [99]. Except for the POH MZM, all these devices were limited in bandwidth for transmission at a maximum line rate of only 20 Gbit/s [96]. With the POH MZM used in [93], line rates up to 128 Gbit/s at temperatures down to 2.6 K could be demonstrated. However, POH MZM inherently feature high optical losses. The SOH device platform combining the high EO coefficient of the EO materials with low optical loss [23], [24] is uniquely suited for emerging applications at cryogenic temperatures.

For cryogenic operation of SOH devices, two challenges have to be addressed. The first issue is specific to RC-SOH devices as the doped silicon slabs are affected by carrier freeze-out. At low temperatures, the carriers stay localized at the dopant atoms. As a consequence, the slab resistance increases, and

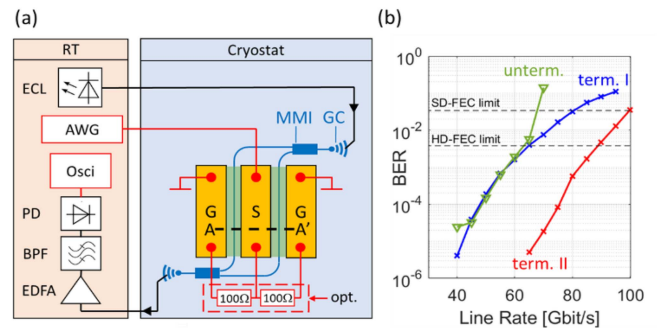


Fig. 11. Schematic of a high-speed cryogenic transmission experiment. (a) An SOH MZM operates at an ambient temperature of 11 K. An arbitrary waveform generator (AWG) operating at RT simulates the cryogenic electronics and is electrically connected to the MZM, which may be electrically terminated with a 50Ω impedance. Light is coupled from an external-cavity laser (ECL) to and from the MZM using grating couplers (GC). The output fiber is connected to an erbium-doped fiber amplifier (EDFA). Amplified spontaneous emission (ASE) noise from the EDFA is filtered by a bandpass filter (BPF). The optical signal is received by a high-speed photodiode (PD), and the electrical waveform is recorded by a real time oscilloscope (Osci.). The recorded data are processed offline by a digital signal processing (DSP) chain, and the bit error ratio (BER) is calculated. (b) Measured BER vs. line rate for terminated (term. I) and unterminated (unterm.) operation. After doubling the drive voltage (term. II), a BER below the threshold for soft decision forward error correction with a 20% overhead could be achieved at a line rate of 100 Gbit/s. Both hard decision FEC limits (HD-FEC) and soft decision limits (SD-FEC) are shown as dashed lines. (Figure adapted from [102]).

the bandwidth of the device decreases. This problem can be overcome by using appropriately high doping levels. In case of n -type doping, dopant concentrations beyond $5 \times 10^{18} \text{cm}^{-3}$ are referred to as degenerate. Beyond this so-called Mott transition, the doped silicon acts as a metal, with the material's resistivity being constant or even decreasing with temperature in case of sufficiently high doping [100].

Second, during cooldown, the organic electro-optic material experiences high thermal stress that can cause the formation of cracks in the organic film. In order to mitigate this issue, JRD1 was mixed with PMMA in a 1:1 ratio [101], and was used for a first demonstration of an SOH MZM at cryogenic temperatures. A $U_{\pi}L$ of 2 Vmm could be measured at temperatures of 4 K, and a line rate of 50 Gbit/s was shown. With PerkinamineTM Series 5 mixed with amorphous polycarbonate (APC), the first cryo-compatible MZM with a sub-volt U_{π} was demonstrated a year later [102]. With this modulator, PAM4 symbol rates (line rates) of up to 70 GBd (140 Gbit/s) could be demonstrated with a 1 mm long device at a temperature of 11 K [102]. The $U_{\pi}L$ of this device was measured to be 0.9 Vmm. To avoid carrier-freeze-out, the device used in this demonstration relied on a multi-level doping scheme, with doping concentrations close to degeneracy near the slot WG, and well beyond degeneracy further away from it.

To test the high-speed operation of the device at cryogenic temperatures, a data transmission experiment was conducted – the schematic setup is shown in Fig. 11(a) and the main results in Fig. 11(b), indicating data rates of up to 100 Gbit/s at a bit-error ratio (BER) just below the threshold for soft decision forward error correction (SD-FEC) with a 20% coding

overhead. The green curve (unterm.) depicts the performance of the unterminated device. Up to line rates of 65 Gbit/s, the behavior of terminated and unterminated modulators is similar. At higher line rates, the device cannot be considered lumped anymore, and the BER increases. By doubling the drive voltage, line rates of up to 100 Gbit/s with a BER below the SD-FEC limit could be achieved. Both the hard-decision FEC and the SD-FEC limits are shown by black dashed lines.

Moreover, EO modulators are potential candidates for building so-called quantum transducers that convert quantum information from superconducting qubits to quantum states in the optical domain. The optical quantum state can be transmitted over long distances through optical fibers. This is advantageous because the optical signals experience very low loss and are immune against thermal noise.

The first attempt to demonstrate an EO quantum transducer on the SOH platform was presented by Witmer et al. [103]. In this work, the SOH modulator is based on a doubly-resonant scheme in order to enhance the conversion efficiency. The approach utilizes a silicon photonic Fabry-Perot type resonator with the organic EO material SEO125 as a cladding. The silicon resonator is embedded in the planar capacitor of a superconducting aluminum resonator with a resonance frequency of 6.7 GHz.

However, the demonstrated conversion efficiency in the order of 10^{-9} is rather low, primarily due to the low optical pump power used in the experiment. At a higher pump power, the Q-factor of the microwave resonator is significantly reduced due to the absorption of scattered pump light by the superconducting Al, followed by the breaking of Cooper pairs and the generation of quasi-particles with long lifetimes.

By using NbTiN or NbN instead of Al, the effect of scattered light on a superconductor might be significantly reduced, potentially increasing the conversion efficiency by several orders of magnitude. Moreover, by using Si slot waveguides, one could further increase the efficiency of the SOH transducer.

D. Emerging Applications of Nonlinear Organic Materials

Spatial light modulator: A very special application of $\chi^{(2)}$ -nonlinear organic materials has been shown in form of a spatial light modulator (SLM) [104]. In a proof-of-concept demonstration, four SLM pixels, arranged in an array (pixel size $390 \mu\text{m} \times 390 \mu\text{m}$, array dimensions $780 \mu\text{m} \times 780 \mu\text{m}$), are voltage-controlled in their transmittivity. Each pixel consists of interdigitated metallic electrodes covered with a nonlinear organic slab (JRD1 mixed with PMMA), which is surrounded by air above and by SiO_2 below. If a center electrode finger has a positive potential, then the two neighboring electrodes have a negative polarity. Using these electrodes, a voltage $U_{\text{pol}} \equiv V_{\text{pol}}$ poles the organic material in-plane, i.e., the poling axis is essentially parallel to the device surface along the z -axis in Fig. 12. A periodically poled organic layer results, where the sign of the electro-optic coefficient alternates between $+|r_{33}|$ and $-|r_{33}|$ with respect to the z -direction.

If then an electric drive field $E_d = \{V_{\text{DC}}/w_{\text{gap}}, V_{\text{AC}}/w_{\text{gap}}\}$ is applied to these interdigitated electrodes, a refractive index change $\Delta n_{\text{EO, idgt}} = -\frac{1}{2}n_{\text{EO}}^3(\pm|r_{33}|)(\pm|E_d|)$ results, (3),

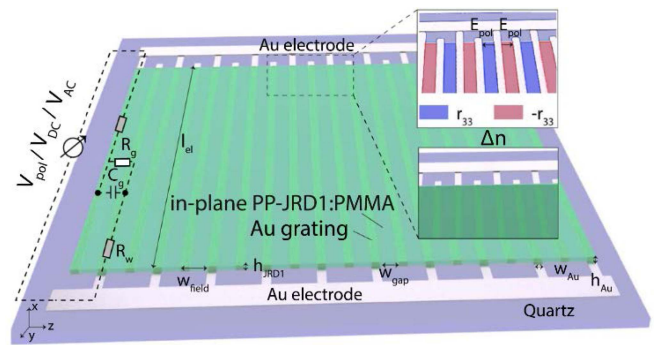


Fig. 12. Array element of a spatial light modulator, comprising a metallic grating and an organic JRD1:PMMA slab with tunable refractive index. Light in a range $\lambda_0 = (1100 \dots 1600) \text{ nm}$ is linearly polarized along the z -direction (at right angle to the grating fingers), shines perpendicularly on the slab and is diffracted by the tunable grating into grating orders. At certain diffraction angles, a guided mode is excited in the organic slab, and the grating scatters the guided light back. Otherwise, the light is transmitted through grating and slab. Data: Array spacing $w_{\text{field}} = (0.8 \dots 1.4) \mu\text{m}$, electrode length $l_{\text{el}} = 390 \mu\text{m}$, $h_{\text{JRD1}} = 690 \text{ nm}$, $w_{\text{gap}} = 1.2 \mu\text{m}$, $w_{\text{Au}} = 200 \text{ nm}$, $h_{\text{Au}} = (40 \dots 50) \text{ nm}$, poling voltage $U_{\text{pol}} \equiv V_{\text{pol}} = 100 \text{ V}$, DC and AC drive voltages $U_d = \{V_{\text{DC}}, V_{\text{AC}}\}$, thin film (Teng-Man ellipsometry @ 1310 nm) $r_{33}^{\text{JRD1}} = 100 \text{ pm/V}$. (Figure adapted from [104]).

which is essentially the same in all unit cells of the grating. A beam of light, linearly polarized along the z -axis and impinging perpendicularly to the grating plane, is diffracted into grating orders, which may or may not excite guided slab modes, depending on the angle of diffraction. The guided light is scattered back, interferes with the incident light, and creates a standing wave, i.e., a resonance [104], [105], [106]. By varying the drive field $|E_d|$, the grating can be tuned to different resonance frequencies, thereby changing the pixel transmittivity between its minimum and its maximum. Because the pixels can be driven individually with a maximum frequency of 50 MHz, the RF domain may be linked with pixels having different spatial positions.

Silicon-organic hybrid laser (SOH laser): The basic concept of SOH integration is to combine highly scalable silicon photonics with organic materials that offer optical functionalities complementary to those of silicon. This approach cannot only be applied to electro-optic modulators, as discussed in the previous sections, but also to laser sources based on dye-doped organic materials [107], and it is not limited to silicon photonics, but can also be expanded to the silicon-nitride (Si_3N_4) platform [108]. Experimentally demonstrated SOH lasers relied on strip and slot waveguides of 4.8 mm length, and were fabricated on an SOI wafer [107]. As illustrated in Fig. 13, the waveguides were embedded into an active organic cladding consisting of a matrix of poly(methyl methacrylate) (PMMA) doped with the commercially available dye IR26, which has a maximum fluorescence at 1150 nm. For enabling laser operation in a wide wavelength range, the wavelength-selective Bragg reflectors shown in Fig. 13(a) are omitted, and the laser cavity was simply formed by cleaved waveguide facets (4. . . 8% power reflection) and by residual reflections from on-chip grating couplers. In a proof-of-concept experiment, the devices were pumped with a pulsed laser having a wavelength of 1064 nm, an FWHM pulse duration of 0.9 ns, and a pulse energy of up to 1.2 mJ at a

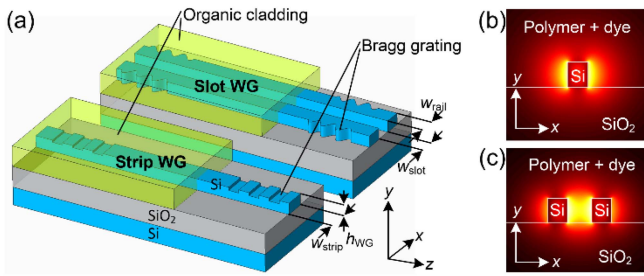


Fig. 13. SOH laser concept. (a) Light is guided by SOI strip or slot waveguides. Optical gain is provided by a fluorescent organic cladding material which covers the strip or fills the slot. The optical pump is either launched from above or injected into the waveguide at one of the facets. Bragg reflectors provide wavelength-selective optical feedback. (b) Dominant electric field component (E_x) of the fundamental quasi-TE mode for a narrow strip waveguide. (c) Dominant electric field component (E_x) of the fundamental quasi-TE mode for a slot waveguide. (Adapted from [107]).

repetition rate of 13.7 Hz. The emitted laser pulses are 0.6 ns wide, much longer than the cavity round-trip time. The effective lifetime of the excited state amounts to 10 ps and is much shorter than the durations of pump and emission pulses, so the lasing is close to steady-state.

Pulsed room-temperature lasing with on-chip peak output powers of up to 1.1 W at a wavelength of 1310 nm was achieved.

Si₃N₄-organic hybrid laser (SiNOH laser): Expanding hybrid integration to the silicon-nitride platform opens a path towards visible-wavelength devices. Especially interesting are disposable sensors for point-of-care analysis of body liquids outside the laboratory, where visible light is favored due to reduced absorption in aqueous biological samples. Such sensors, however, require cost-effective laser sources which can be integrated directly on the chip.

Here, the combination of silicon nitride waveguides with light emitting organic cladding materials comes into play, leading to so-called SiNOH lasers (Si₃N₄-organic hybrid). They can be produced cost-effectively in large quantities by complementing highly scalable passive Si₃N₄ waveguides with appropriate light-emitting materials [108], [119]. More specifically, the necessary laser and sensing waveguides are fabricated in a first step, using standard lithographic processes, and the laser waveguide structures are then covered, similarly as with the strip WG in Fig. 13(a), with an organic cladding material PMMA, which may, e.g., rely on pyrromethene 597 (PM 597) as a light-emitting dye. The absorption peak of PM 597 is at 523 nm, and the emission peak at 567 nm. Pyrromethenes [109] offer even better laser action than rhodamine dyes. The SiNOH lasers are pumped with external pulsed light sources, such as LED or laser diodes, and the signal of the co-integrated sensors are detected by a simple camera. The functionality of SiNOH lasers in biosensors was demonstrated in a proof-of-concept experiment [119].

VI. CONCLUSION

We reviewed the current state of the art related to a silicon-on-insulator (SOI) technology in combination with nonlinear organic materials, leading to high-speed and energy-efficient

silicon-organic hybrid (SOH) Mach-Zehnder modulators. Possible stability issues of the organic material are being addressed, and the associated solutions were elaborated. We derived and discussed relevant modulator metrics. After a comparison of different modulator implementations using organic materials, we reported typical applications, mainly in the framework of optical communications and cryoelectronics. Further, we referred to emerging applications in metrology and sensing, covering also hybrid organic lasers.

REFERENCES

- [1] N. Margalit et al., "Perspective on the future of silicon photonics and electronics," *Appl. Phys. Lett.*, vol. 118, Jun. 2021, Art. no. 220501, doi: [10.1063/5.0050117](https://doi.org/10.1063/5.0050117).
- [2] J. Witzens, T. Baehr-Jones, and M. Hochberg, "Design of transmission line driven slot waveguide Mach-Zehnder interferometers and application to analog optical links," *Opt. Exp.*, vol. 18, no. 16, pp. 16902–16928, Aug. 2010, doi: [10.1364/OE.18.016902](https://doi.org/10.1364/OE.18.016902).
- [3] J. Witzens, "High-speed silicon photonics modulators," *Proc. IEEE*, vol. 106, no. 12, pp. 2158–2182, Dec. 2018, doi: [10.1109/JPROC.2018.2877636](https://doi.org/10.1109/JPROC.2018.2877636).
- [4] W. M. J. Green, M. J. Rooks, L. Sekaric, and Y. A. Vlasov, "Ultra-compact, low RF power, 10 Gb/s silicon Mach-Zehnder modulator," *Opt. Exp.*, vol. 15, no. 25, pp. 17106–17113, Dec. 2007, doi: [10.1364/OE.15.017106](https://doi.org/10.1364/OE.15.017106).
- [5] A. C. Turner-Foster et al., "Ultrashort free-carrier lifetime in low-loss silicon nanowaveguides," *Opt. Exp.*, vol. 18, no. 4, pp. 3582–3591, Feb. 2010, doi: <https://doi.org/10.1364/OE.18.003582>.
- [6] L. Liao et al., "40 Gbit/s silicon optical modulator for high-speed applications," *Electron. Lett.*, vol. 43, no. 22, pp. 1195–1197, Oct. 2007, doi: [10.1049/el:20072253](https://doi.org/10.1049/el:20072253).
- [7] Md. S. Alam et al., "Net 220 Gbps/λ IM/DD transmission in O-band and C-band with silicon photonic traveling-wave MZM," *J. Lightw. Technol.*, vol. 39, no. 13, pp. 4270–4278, Jul. 2021, doi: [10.1109/JLT.2021.3074096](https://doi.org/10.1109/JLT.2021.3074096).
- [8] S. Wolf et al., "Silicon-organic hybrid (SOH) Mach-Zehnder modulators for 100 Gbit/s on-off keying," *Sci. Rep.*, vol. 8, Apr. 2018, Art. no. 2598, doi: [10.1038/s41598-017-19061-8](https://doi.org/10.1038/s41598-017-19061-8).
- [9] J.-M. Brosi et al., "High-speed low-voltage electro-optic modulator with a polymer-infiltrated silicon photonic crystal waveguide," *Opt. Exp.*, vol. 16, no. 6, pp. 4177–4191, Mar. 2008, doi: [10.1364/OE.16.004177](https://doi.org/10.1364/OE.16.004177).
- [10] P. Steglich et al., "Silicon-organic hybrid photonics: An overview of recent advances, electro-optical effects and CMOS integration concepts," *J. Phys. Photon.*, vol. 3, Apr. 2021, Art. no. 022009, doi: [10.1088/2515-7647/abd7cf](https://doi.org/10.1088/2515-7647/abd7cf).
- [11] C. Koos et al., "Silicon-organic hybrid (SOH) and plasmonic-organic hybrid (POH) integration," *J. Lightw. Technol.*, vol. 34, no. 2, pp. 256–268, Jan. 2016, doi: [10.1109/JLT.2015.2499763](https://doi.org/10.1109/JLT.2015.2499763).
- [12] P. N. Prasad and D. J. Williams, *Introduction to Nonlinear Optical Effects in Molecules and Polymers*. New York, NY, USA: Wiley, Jan. 1991, doi: [10.1002/pi.4990250317](https://doi.org/10.1002/pi.4990250317).
- [13] J. Wolff and R. Wortmann, "Organic materials for second-order nonlinear optics," *Adv. Phys. Org. Chem.*, vol. 32, pp. 121–217, Jan. 1999, doi: [10.1016/S0065-3160\(08\)60007-6](https://doi.org/10.1016/S0065-3160(08)60007-6).
- [14] L. R. Dalton, P. A. Sullivan, and D. H. Bale, "Electric field poled organic electro-optic materials: State of the Art and future prospects," *Chem. Rev.*, vol. 110, no. 1, pp. 25–55, Oct. 2009, doi: [10.1021/cr9000429](https://doi.org/10.1021/cr9000429).
- [15] S. R. Marder, D. N. Beratan, and L.-T. Cheng, "Approaches for optimizing the first electronic hyperpolarizability of conjugated organic molecules," *Science*, vol. 252, no. 5002, pp. 103–106, Apr. 1991, doi: [10.1126/science.252.5002.103](https://doi.org/10.1126/science.252.5002.103).
- [16] S. R. Marder et al., "Relation between bond-length alternation and second electronic hyperpolarizability of conjugated organic molecules," *Science*, vol. 261, no. 5118, pp. 186–189, Jul. 1993, doi: [10.1126/science.261.5118.186](https://doi.org/10.1126/science.261.5118.186).
- [17] K. D. Singer, M. G. Kuzyk, and J. E. Sohn, "Second-order nonlinear-optical processes in orientationally ordered materials: Relationship between molecular and macroscopic properties," *J. Opt. Soc. Amer. B*, vol. 4, no. 6, pp. 968–976, Jun. 1987, doi: [10.1364/JOSAB.4.000968](https://doi.org/10.1364/JOSAB.4.000968).

- [18] D. M. Burland, R. D. Miller, and C. A. Walsh, "Second-order nonlinearity in poled-polymer systems," *Chem. Rev.*, vol. 94, no. 1, pp. 31–75, Jan. 1994, doi: [10.1021/cr00025a002](https://doi.org/10.1021/cr00025a002).
- [19] F. Ullah, N. Deng, and F. Qiu, "Recent progress in electro-optic polymer for ultra-fast communication," *Photonix*, vol. 2, no. 1, pp. 1–18, Dec. 2021, doi: [10.1186/s43074-021-00036-y](https://doi.org/10.1186/s43074-021-00036-y).
- [20] S. Pascal et al., "Design of near-infrared-absorbing unsymmetrical polymethine dyes with large quadratic hyperpolarizabilities," *Chem. Mater.*, vol. 30, no. 10, pp. 3410–3418, Apr. 2018, doi: [10.1021/acs.chemmater.8b00960](https://doi.org/10.1021/acs.chemmater.8b00960).
- [21] S. J. Benight, D. H. Bale, B. C. Olbricht, and L. R. Dalton, "Organic electro-optics: Understanding material structure/function relationships and device fabrication issues," *J. Mater. Chem.*, vol. 40, pp. 7466–7475, Jun. 2009, doi: [10.1039/B905368A](https://doi.org/10.1039/B905368A).
- [22] I. Taghavi et al., "Polymer modulators in silicon photonics: Review and projections," *Nanophotonics*, vol. 11, no. 17, pp. 3855–3871, Jul. 2022, doi: [10.1515/nanoph-2022-0141](https://doi.org/10.1515/nanoph-2022-0141).
- [23] C. Kieninger et al., "Silicon-organic hybrid (SOH) Mach-Zehnder modulators for 100 Gb/s PAM4 signaling with sub-1 dB phase-shifter loss," *Opt. Exp.*, vol. 28, no. 17, pp. 24693–24707, Aug. 2020, doi: [10.1364/OE.390315](https://doi.org/10.1364/OE.390315).
- [24] C. Kieninger et al., "Ultra-high electro-optic activity demonstrated in a silicon-organic hybrid modulator," *Optica*, vol. 5, no. 6, pp. 739–748, Jun. 2018, doi: [10.1364/OPTICA.5.000739](https://doi.org/10.1364/OPTICA.5.000739).
- [25] C. Kieninger et al., "Demonstration of long-term thermally stable silicon-organic hybrid modulators at 85 °C," *Opt. Exp.*, vol. 26, no. 21, pp. 27955–27964, Oct. 2018, doi: [10.1364/OE.26.027955](https://doi.org/10.1364/OE.26.027955).
- [26] C. Pecinovsky, B. Johnson, and G. Ramann, "Non-linear optical chromophores having a diamondoid group attached thereto, methods of preparing the same, and uses thereof," US patent 2021/0405504 A1, Dec. 30, 2021.
- [27] H. Xu et al., "Ultrahigh electro-optic coefficients, high index of refraction, and long-term stability from Diels-Alder cross-linkable binary molecular glasses," *Chem. Mater.*, vol. 32, pp. 1408–1421, Jan. 2020, doi: [10.1021/acs.chemmater.9b03725](https://doi.org/10.1021/acs.chemmater.9b03725).
- [28] X. Zhang et al., "Novel photo-cross-linkable polymer bearing spindle-type chromophores for second-order non-linear optical materials," *J. Mater. Sci.*, vol. 46, pp. 4458–4464, Jan. 2011, doi: [10.1007/s10853-011-5338-6](https://doi.org/10.1007/s10853-011-5338-6).
- [29] Y. Tominarie, T. Yamada, T. Kaji, C. Yamada, and A. Otomo, "Photostability of organic electro-optic polymer under practical high intensity continuous-wave 1550 nm laser irradiation," *Appl. Phys.*, vol. 60, Sep. 2021, Art. no. 101002, doi: [10.35848/1347-4065/ac235a](https://doi.org/10.35848/1347-4065/ac235a).
- [30] C. Hoessbacher et al., "Plasmonic-organic-hybrid (POH) modulators – A powerful platform for next-generation integrated circuits," in *Proc. OSA Adv. Photon. Congr.*, 2021, paper IW1B.5.
- [31] O. S. Gebizlioglu, "Generic reliability assurance requirements for optoelectronic devices used in telecommunications equipment," Telcordia Standard GR-468-CORE, 2004. [Online]. Available: <https://api.semanticscholar.org/CorpusID:170077028>
- [32] C. Eschenbaum et al., "Thermally stable silicon-organic hybrid (SOH) Mach-Zehnder modulator for 140 Gb/s PAM4 transmission with sub-1 V drive signals," in *Proc. Eur. Conf. Opt. Commun.*, 2022, pp. 1–4.
- [33] H. Miura et al., "High thermal stability 40 GHz electro-optic polymer modulators," *Opt. Exp.*, vol. 25, no. 23, pp. 28643–28649, Nov. 2017, doi: [10.1364/OE.25.028643](https://doi.org/10.1364/OE.25.028643).
- [34] A. Schwarzenberger et al., "First demonstration of a silicon-organic hybrid (SOH) modulator based on a long-term-stable crosslinked electro-optic material," in *Proc. Eur. Conf. Opt. Commun.*, 2023, paper We.A.4.2.
- [35] A. E.-J. Lim et al., "Review of silicon photonics foundry efforts," *IEEE J. Sel. Topics Quantum Electron.*, vol. 20, no. 4, pp. 405–416, Jul./Aug. 2014, doi: [10.1109/STQE.2013.2293274](https://doi.org/10.1109/STQE.2013.2293274).
- [36] S. Y. Siew et al., "Review of silicon photonics technology and platform development," *J. Lightw. Technol.*, vol. 39, no. 13, pp. 4374–4389, Jul. 2021, doi: [10.1109/JLT.2021.3066203](https://doi.org/10.1109/JLT.2021.3066203).
- [37] S. Liu et al., "Thermo-optic phase shifters based on silicon-on-insulator platform: State-of-the-art and a review," *Front. Optoelectron.*, vol. 15, no. 9, pp. 1–21, Apr. 2022, doi: [10.1007/s12200-022-00012-9](https://doi.org/10.1007/s12200-022-00012-9).
- [38] D. Ahn et al., "High performance, waveguide integrated Ge photodetectors," *Opt. Exp.*, vol. 15, no. 7, pp. 3916–3921, Apr. 2007, doi: [10.1364/OE.15.003916](https://doi.org/10.1364/OE.15.003916).
- [39] L. Carroll et al., "Photonic packaging: Transforming silicon photonic integrated circuits into photonic devices," *Appl. Sci.*, vol. 6, no. 12, Dec. 2016, Art. no. 426, doi: [10.3390/app6120426](https://doi.org/10.3390/app6120426).
- [40] D. Liang, G. Roelkens, R. Baets, and J. Bowers, "Hybrid integrated platforms for silicon photonics," *Materials*, vol. 3, no. 3, pp. 1782–1802, Mar. 2010, doi: [10.3390/ma3031782](https://doi.org/10.3390/ma3031782).
- [41] H. Rong et al., "A continuous-wave Raman silicon laser," *Nature*, vol. 433, pp. 725–728, Feb. 2005, doi: [10.1038/nature03346](https://doi.org/10.1038/nature03346).
- [42] W. Jin et al., "Benzocyclobutene barrier layer for suppressing conductance in nonlinear optical devices during electric field poling," *Appl. Phys. Lett.*, vol. 104, no. 24, Jun. 2014, Art. no. 243304, doi: [10.1063/1.4884829](https://doi.org/10.1063/1.4884829).
- [43] A. Teichler, J. Perelaer, and U.S. Schubert, "Inkjet printing of organic electronics – comparison of deposition techniques and state-of-the-art developments," *J. Mater. Chem., C*, vol. 1, pp. 1910–1925, Dec. 2012, doi: [10.1039/c2tc00255h](https://doi.org/10.1039/c2tc00255h).
- [44] S. Ummethala et al., "THz-to-optical conversion in wireless communications using an ultra-broadband plasmonic modulator," *Nature Photon.*, vol. 13, pp. 519–524, Aug. 2019, doi: [10.1038/s41566-019-0475-6](https://doi.org/10.1038/s41566-019-0475-6).
- [45] W. Heni et al., "Nonlinearities of organic electro-optic materials in nanoscale slots and implications for the optimum modulator design," *Opt. Exp.*, vol. 25, no. 3, pp. 2627–2653, Feb. 2017, doi: [10.1364/OE.25.002627](https://doi.org/10.1364/OE.25.002627).
- [46] R. Palmer et al., "Low-loss silicon strip-to-slot mode converters," *IEEE Photon. J.*, vol. 5, no. 1, Feb. 2013, Art. no. 2200409, doi: [10.1109/JPHOT.2013.2239283](https://doi.org/10.1109/JPHOT.2013.2239283).
- [47] H. Zwickel et al., "Silicon-organic hybrid (SOH) modulators for intensity-modulation/direct-detection links with line rates of up to 120 Gbit/s," *Opt. Exp.*, vol. 25, no. 20, pp. 23784–23800, Oct. 2017, doi: [10.1364/OE.25.023784](https://doi.org/10.1364/OE.25.023784).
- [48] H. Zwickel et al., "Verified equivalent-circuit model for slot-waveguide modulators," *Opt. Exp.*, vol. 28, no. 9, pp. 12951–12976, Apr. 2020, doi: [10.1364/OE.383120](https://doi.org/10.1364/OE.383120).
- [49] S. Ummethala et al., "Hybrid electro-optic modulator combining silicon photonic slot waveguides with high-k radio-frequency slotlines," *Optica*, vol. 8, no. 4, pp. 511–519, Apr. 2021, doi: [10.1364/OPTICA.411161](https://doi.org/10.1364/OPTICA.411161).
- [50] Z. Q. Shi, Q. X. Jia, and W. A. Anderson, "Electrical and dielectric properties of thin film BaTiO₃ capacitors deposited by radio frequency magnetron sputtering," *J. Vac. Sci. Technol. A*, vol. 10, no. 4, pp. 733–736, Jul. 1992, doi: [10.1116/1.578153](https://doi.org/10.1116/1.578153).
- [51] G.-W. Lu et al., "High-temperature-resistant silicon-polymer hybrid modulator operating at up to 200 Gbit s⁻¹ for energy-efficient data-centres and harsh-environment applications," *Nature Commun.*, vol. 11, Oct. 2020, Art. no. 4224, doi: [10.1038/s41467-020-18005-7](https://doi.org/10.1038/s41467-020-18005-7).
- [52] S. Yokoyama, G.-W. Lu, X. Cheng, F. Qiu, and A. M. Spring, "110 Gbit/s on-off keying transmitter based on a single-drive polymer modulator," in *Proc. Opt. Fiber Commun. Conf. Exhib.*, 2019, paper Tu2H.
- [53] S. K. Tolpygo, "Superconductor digital electronics: Scalability and energy efficiency issues," *Low Temp. Phys.*, vol. 42, no. 5, pp. 361–379, May 2016, doi: [10.1063/1.4948618](https://doi.org/10.1063/1.4948618).
- [54] T. E. Roth, R. Ma, and W. C. Chew, "The transmon qubit for electromagnetics engineers: An introduction," *IEEE Antennas Propag. Mag.*, vol. 65, no. 2, pp. 8–20, Apr. 2023, doi: [10.1109/map.2022.3176593](https://doi.org/10.1109/map.2022.3176593).
- [55] R. Kleiner, D. Koelle, F. Ludwig, and J. Clarke, "Superconducting quantum interference devices: State of the art and applications," *Proc. IEEE*, vol. 92, no. 10, pp. 1534–1548, Oct. 2004, doi: [10.1109/jproc.2004.833655](https://doi.org/10.1109/jproc.2004.833655).
- [56] K. Irwin and G. Hilton, "Transition-edge sensors," in *Cryogenic Particle Detection. Topics in Applied Physics*, C. Enss Ed., Berlin, Heidelberg, Germany: Springer, vol. 99, 2005, pp. 63–150, doi: [10.1007/10933596_3](https://doi.org/10.1007/10933596_3).
- [57] B. A. Mazin, "Microwave kinetic inductance detectors," in *The WSPC Handbook of Astronomical Instrumentation*, Singapore: World Scientific, 2021, pp. 35–52, doi: [10.1142/9789811203787_0002](https://doi.org/10.1142/9789811203787_0002).
- [58] I. E. Zadeh et al., "Superconducting nanowire single-photon detectors: A perspective on evolution, state-of-the-art, future developments, and applications," *Appl. Phys. Lett.*, vol. 118, no. 19, May 2021, Art. no. 190502, doi: [10.1063/5.0045990](https://doi.org/10.1063/5.0045990).
- [59] H. J. Kimble, "The quantum internet," *Nature*, vol. 453, no. 7198, pp. 1023–1030, Jun. 2008, doi: [10.1038/nature0712](https://doi.org/10.1038/nature0712).
- [60] V. Scarani et al., "The security of practical quantum key distribution," *Rev. Mod. Phys.*, vol. 81, no. 3, pp. 1301–1350, Sep. 2009, doi: [10.1103/revmodphys.81.1301](https://doi.org/10.1103/revmodphys.81.1301).
- [61] A. Youssefi et al., "A cryogenic electro-optic interconnect for superconducting devices," *Nature Electron.*, vol. 4, pp. 326–332, May 2021, doi: [10.1038/s41928-021-00570-4](https://doi.org/10.1038/s41928-021-00570-4).
- [62] R.W. Boyd, *Nonlinear Optics*, 3rd ed. New York, NY, USA: Academic (imprint of Elsevier), 2008, ch. 11.

- [63] H. Kogelnik, "Theory of dielectric waveguides," in *Integrated Optics*. Berlin, Germany: Springer, 1975, pp. 13–81.
- [64] R. Palmer, "Silicon photonic modulators for low-power applications," Ph.D. dissertation, Karlsruhe Inst. Technol., Germany, 2015, doi: [10.5445/KSP/1000047154](https://doi.org/10.5445/KSP/1000047154).
- [65] Y. Shi, L. Yan, and A. E. Willner, "High-speed electrooptic modulator characterization using optical spectrum analysis," *J. Lightw. Technol.*, vol. 21, no. 10, pp. 2358–2367, Oct. 2003, doi: [10.1109/JLT.2003.818162](https://doi.org/10.1109/JLT.2003.818162).
- [66] S. Ummethala, "Plasmonic-organic and silicon-organic hybrid modulators for high-speed signal processing," Ph.D. dissertation, Karlsruhe Inst. Technol., Germany, 2021, doi: [10.5445/IR/1000136059](https://doi.org/10.5445/IR/1000136059).
- [67] J.-M. Brosi, "Slow-light photonic crystal devices for high-speed optical signal processing," Ph.D. dissertation, Karlsruhe Inst. Technol., Germany, 2009, doi: [10.5445/KSP/1000009905](https://doi.org/10.5445/KSP/1000009905).
- [68] C. Koos, "Nanophotonic devices for linear and nonlinear optical signal processing," Ph.D. dissertation, Karlsruhe Inst. Technol., Germany, 2007, doi: [10.5445/KSP/1000007120](https://doi.org/10.5445/KSP/1000007120).
- [69] S. H. Lin and S.-Y. Wang, "High-throughput GaAs PIN electrooptic modulator with a 3-dB bandwidth of 96 GHz at 1.3 μm ," *Appl. Opt.*, vol. 26, no. 9, pp. 1696–1700, May 1987, doi: [10.1364/AO.26.001696](https://doi.org/10.1364/AO.26.001696).
- [70] S. Y. Wang and S. H. Lin, "High speed III-V electro-optic waveguide modulators at $\lambda = 1.3 \mu\text{m}$," *J. Lightw. Technol.*, vol. 6, no. 6, pp. 758–771, Jun. 1988, doi: [10.1109/50.4064](https://doi.org/10.1109/50.4064).
- [71] R. G. Walker, "High-speed III-V semiconductor intensity modulators," *IEEE J. Quantum Electron.*, vol. 27, no. 3, pp. 654–667, Mar. 1991, doi: [10.1109/3.81374](https://doi.org/10.1109/3.81374).
- [72] *IEEE Standard for Ethernet Amendment 4: Physical Layer Specifications and Management Parameters for 100 Gb/s, 200 Gb/s, and 400 Gb/s Electrical Interfaces Based on 100 Gb/s Signaling*, IEEE Standard 802.3ck-2022, Dec. 28, 2022, doi: [10.1109/IEEESTD.2022.9999414](https://doi.org/10.1109/IEEESTD.2022.9999414).
- [73] C.-J. Chung et al., "Towards a fully packaged high-performance RF sensor featuring slotted photonic crystal waveguides," *Proc. SPIE*, vol. 9747, pp. 272–283, 2016, doi: [10.1117/12.2213557](https://doi.org/10.1117/12.2213557).
- [74] S. Wolf et al., "Coherent modulation up to 100 GBd 16QAM using silicon-organic hybrid (SOH) devices," *Opt. Exp.*, vol. 26, no. 1, pp. 220–232, 2018, doi: [10.1364/OE.26.000220](https://doi.org/10.1364/OE.26.000220).
- [75] G.-W. Lu, H. Sato, J. Mao, and S. Yokoyama, "Silicon-polymer hybrid modulators with high-temperature resistance for energy-efficient data centers," in *Proc. Opto-Electron. Commun. Conf.*, 2023, pp. 1–3, doi: [10.1109/OECC56963.2023.10209709](https://doi.org/10.1109/OECC56963.2023.10209709).
- [76] S. Yokoyama, G. W. Lu, H. Miura, F. Qiu, and A. M. Spring, "High temperature resistant 112 Gbit/s PAM4 modulator based on electro-optic polymer modulator," in *Proc. IEEE Eur. Conf. Opt. Commun.*, 2018, pp. 1–3, doi: [10.1109/ECOC.2018.8535460](https://doi.org/10.1109/ECOC.2018.8535460).
- [77] S. Wolf et al., "DAC-less amplifier-less generation and transmission of QAM signals using sub-volt silicon-organic hybrid modulators," *J. Light. Technol.*, vol. 33, no. 7, pp. 1425–1432, Apr. 2015, doi: [10.1109/JLT.2015.2394511](https://doi.org/10.1109/JLT.2015.2394511).
- [78] J. Fujikata, H. Sato, A. Bannaron, G. W. Lu, and S. Yokoyama, "High-performance EO polymer/Si and InP nano-hybrid optical modulators in O-band and C-band wavelengths," in *Proc. IEEE Opt. Fiber Commun. Conf. Exhib.*, 2023, pp. 1–3, doi: [10.1364/OFC.2023.Tu3C.4](https://doi.org/10.1364/OFC.2023.Tu3C.4).
- [79] H. Mardoyan et al., "Generation and transmission of 160-GBaud QPSK coherent signals using a dual-drive plasmonic-organic hybrid IQ modulator on silicon photonics," in *Proc. Opt. Fiber Commun. Conf. Exhib.*, 2022, paper Th1J.5, doi: [10.1364/OFC.2022.Th1J.5](https://doi.org/10.1364/OFC.2022.Th1J.5).
- [80] Q. Hu et al., "Ultrahigh-net-bitrate 363 Gbit/s PAM-8 and 279 Gbit/s polybinary optical transmission using plasmonic Mach-Zehnder modulator," *J. Light. Technol.*, vol. 40, no. 10, pp. 3338–3346, May 2022, doi: [10.1109/JLT.2022.3172246](https://doi.org/10.1109/JLT.2022.3172246).
- [81] M. Burla et al., "500 GHz plasmonic Mach-Zehnder modulator enabling sub-THz microwave photonics," *APL Photon.*, vol. 4, no. 5, May 2019, Art. no. 056106, doi: [10.1063/1.5086868](https://doi.org/10.1063/1.5086868).
- [82] Y. Hirano et al., "Demonstration of an optical phased array using electro-optic polymer phase shifters," *Jpn. J. Appl. Phys.*, vol. 57, no. 3S2, Jan. 2018, Art. no. 03EH09, doi: [10.7567/JJAP.57.03EH09](https://doi.org/10.7567/JJAP.57.03EH09).
- [83] Y. Hirano et al., "High-speed optical-beam scanning by an optical phased array using electro-optic polymer waveguides," *IEEE Photon. J.*, vol. 12, no. 2, Apr. 2020, Art. no. 6600807, doi: [10.1109/JPHOT.2020.2981743](https://doi.org/10.1109/JPHOT.2020.2981743).
- [84] M. Lauermann et al., "Integrated optical frequency shifter in silicon-organic hybrid (SOH) technology," *Opt. Exp.*, vol. 24, no. 11, pp. 11694–11707, May 2016, doi: [10.1364/OE.24.011694](https://doi.org/10.1364/OE.24.011694).
- [85] H. Li et al., "Demonstration of a flexible electro-optic polymer modulator with a low half-wave voltage for ECG signals acquisition," *Opt. Laser Technol.*, vol. 153, Sep. 2022, Art. no. 108253, doi: [10.1016/j.optlastec.2022.108253](https://doi.org/10.1016/j.optlastec.2022.108253).
- [86] H. Li et al., "Fabrication and characterization of electro-optic polymer/silicon hybrid MZI for interrogating small signals from an ECG," *Opt. Commun.*, vol. 539, Apr. 2023, Art. no. 129510, doi: [10.1016/j.optcom.2023.129510](https://doi.org/10.1016/j.optcom.2023.129510).
- [87] H. Li et al., "Low half-wave voltage polymeric electro-optic modulator using CLD-1/PMMA for electrocardiogram (ECG) signal acquisition," *Opt. Exp.*, vol. 31, no. 8, pp. 12072–12082, Mar. 2023, doi: [10.1364/OE.484785](https://doi.org/10.1364/OE.484785).
- [88] A. Shinya et al., "High-speed optical convolutional neural network accelerator with 100 GBaud EO-polymer/Si hybrid optical modulator," in *Proc. Opto-Electron. Commun. Conf.*, 2023, pp. 1–4, doi: [10.1109/OECC56963.2023.10209890](https://doi.org/10.1109/OECC56963.2023.10209890).
- [89] T. Kaji et al., "D-band optical modulators using electro-optic polymer waveguides and non-coplanar patch antennas," *Opt. Exp.*, vol. 31, no. 11, pp. 17112–17121, May 2023, doi: [10.1364/OE.484191](https://doi.org/10.1364/OE.484191).
- [90] T. Kaji et al., "W-band optical modulators using electro-optic polymer waveguides and patch antenna arrays," *Opt. Exp.*, vol. 29, no. 19, pp. 29604–29614, Sep. 2021, doi: [10.1364/OE.434028](https://doi.org/10.1364/OE.434028).
- [91] N. Wada, T. Kaji, T. Yamada, and A. Otomo, "New ICT devices enabled by organic electro-optic polymers," in *Proc. IEEE 23rd Int. Conf. Transparent Opt. Netw.*, 2023, pp. 1–4, doi: [10.1109/IC-TON59386.2023.10207392](https://doi.org/10.1109/IC-TON59386.2023.10207392).
- [92] S. Kamada et al., "Superiorly low half-wave voltage electro-optic polymer modulator for visible photonics," *Opt. Exp.*, vol. 30, no. 11, pp. 19771–19780, May 2022, doi: [10.1364/OE.456271](https://doi.org/10.1364/OE.456271).
- [93] P. Habegger et al., "Plasmonic 100-GHz electro-optic modulators for cryogenic applications," in *Proc. Eur. Conf. Opt. Commun.*, 2022, paper Tu1G.1.
- [94] U. Chakraborty et al., "Cryogenic operation of silicon photonic modulators based on the DC Kerr effect," *Optica*, vol. 7, no. 4, pp. 1385–1390, Jul. 2020, doi: [10.1364/OPTICA.403178](https://doi.org/10.1364/OPTICA.403178).
- [95] P. Pintus et al., "Ultralow voltage, high-speed, and energy-efficient cryogenic electro-optic modulator," *Optica*, vol. 9, no. 10, pp. 1176–1182, Oct. 2022, doi: [10.1364/OPTICA.463722](https://doi.org/10.1364/OPTICA.463722).
- [96] F. Eltes et al., "An integrated optical modulator operating at cryogenic temperatures," *Nature Mater.*, vol. 19, pp. 1164–1168, Jul. 2020, doi: [10.1038/s41563-020-0725-5](https://doi.org/10.1038/s41563-020-0725-5).
- [97] M. Gehl et al., "Operation of high-speed silicon photonic micro-disk modulators at cryogenic temperatures," *Optica*, vol. 4, no. 3, pp. 374–382, Mar. 2017, doi: [10.1364/OPTICA.4.000374](https://doi.org/10.1364/OPTICA.4.000374).
- [98] H. Gevorgyan et al., "Cryo-compatible, silicon spoked-ring modulator in a 45 nm CMOS platform for 4 K-to-room-temperature optical links," in *Proc. IEEE Opt. Fiber Commun. Conf. Exhib.*, 2021, pp. 1–3, doi: [10.1364/OFC.2021.M3B.3](https://doi.org/10.1364/OFC.2021.M3B.3).
- [99] B. S. Lee et al., "High-performance integrated graphene electro-optic modulator at cryogenic temperature," *Nanophotonics*, vol. 10, no. 1, pp. 99–104, Sep. 2020, doi: [10.1515/nanoph-2020-0363](https://doi.org/10.1515/nanoph-2020-0363).
- [100] C. Yamanouchi et al., "Electric conduction in phosphorous doped silicon at low temperatures," *JPSJ*, vol. 22, no. 3, pp. 859–864, Mar. 1967, doi: [10.1143/JPSJ.22.859](https://doi.org/10.1143/JPSJ.22.859).
- [101] A. Schwarzenberger et al., "Cryogenic operation of a silicon-organic hybrid (SOH) modulator at 50 Gbps and 4K ambient temperature," in *Proc. IEEE Eur. Conf. Opt. Commun.*, 2022, paper Th3B.3.
- [102] A. Schwarzenberger et al., "First demonstration of a cryogenic silicon organic hybrid (SOH) Mach-Zehnder modulator with a sub-1 V π -voltage," in *Proc. CLEO*, 2023, paper STh5C.7.
- [103] J. D. Witmer et al., "A silicon-organic hybrid platform for quantum microwave-to-optical transduction," *Quantum Sci. Technol.*, vol. 5, no. 3, Apr. 2020, Art. no. 034004, doi: [10.1088/2058-9565/ab7eed](https://doi.org/10.1088/2058-9565/ab7eed).
- [104] I.-C. Benea-Chelmsu et al., "Electro-optic spatial light modulator from an engineered organic layer," *Nature Commun.*, vol. 12, Oct. 2021, Art. no. 5928, doi: [10.1038/s41467-021-26035-y](https://doi.org/10.1038/s41467-021-26035-y).
- [105] A. Hessel and A. A. Oliner, "A new theory of Wood's anomalies on optical gratings," *Appl. Opt.*, vol. 4, no. 10, pp. 1275–1297, Oct. 1965.
- [106] S. S. Wang and R. Magnusson, "Theory and applications of guided-mode resonance filters," *Appl. Opt.*, vol. 32, no. 14, pp. 2606–2613, May 1993.
- [107] D. Korn et al., "Lasing in silicon-organic hybrid waveguides," *Nature Commun.*, vol. 7, Mar. 2016, Art. no. 10864, doi: [10.1038/ncomms10864](https://doi.org/10.1038/ncomms10864).

- [108] D. Kohler et al., "Lasing in Si₃N₄-organic hybrid (SiNOH) waveguides," *Opt. Exp.*, vol. 28, no. 4, pp. 5085–5104, Feb. 2020, doi: [10.1364/OE.381572](https://doi.org/10.1364/OE.381572).
- [109] J. B. Prieto, F. L. Arbeloa, V. M. Martinez, T. Arbeloa Lopez, and I. Lopez Arbeloa, "Photophysical properties of the pyromethene 597 dye: Solvent effect," *J. Phys. Chem. A*, vol. 108, no. 26, pp. 5504–5508, Jul. 2004, doi: [10.1021/jp0373898](https://doi.org/10.1021/jp0373898).
- [110] B. Baeuerle et al., "120 Gbd plasmonic Mach-Zehnder modulator with a novel differential electrode design operated at a peak-to-peak drive voltage of 178 mV," *Opt. Exp.*, vol. 27, no. 11, pp. 16823–16832, Jun. 2019, doi: [10.1364/OE.27.016823](https://doi.org/10.1364/OE.27.016823).
- [111] L. R. Dalton et al., "Perspective: Nanophotonic electro-optics enabling THz bandwidths, exceptional modulation and energy efficiencies, and compact device footprints," *APL Mater.*, vol. 11, May 2023, Art. no. 050901, doi: [10.1063/5.0145212](https://doi.org/10.1063/5.0145212).
- [112] J. W. Quilty, "The predicted electro-optic coefficient r_{33} of nonlinear optical polymers containing a range of donor- π -acceptor merocyanine chromophores," *Opt. Mater.*, vol. 52, pp. 173–176, Feb. 2016, doi: [10.1016/j.optmat.2015.12.017](https://doi.org/10.1016/j.optmat.2015.12.017).
- [113] K. D. Singer, M. G. Kuzyk, and J. E. Sohn, "Second-order nonlinear-optical processes in orientationally ordered materials: Relationship between molecular and macroscopic properties," *J. Opt. Soc. Am. B*, vol. 4, no. 6, pp. 968–976, Jun. 1987, doi: [10.1364/JOSAB.4.000968](https://doi.org/10.1364/JOSAB.4.000968).
- [114] C. Sun et al., "Single-chip microprocessor that communicates directly using light," *Nature*, vol. 528, no. 24, pp. 534–538, Dec. 2015, doi: [10.1038/nature16454](https://doi.org/10.1038/nature16454).
- [115] Y. Xu et al., "Hybrid external-cavity lasers (ECL) using photonic wire bonds as coupling elements," *Sci. Rep.*, vol. 11, Aug. 2021, Art. no. 16426, doi: [10.1038/s41598-021-95981-w](https://doi.org/10.1038/s41598-021-95981-w).
- [116] Y. Xu et al., "3D-printed facet-attached microlenses for advanced photonic system assembly," *Light: Adv. Manuf.*, vol. 4, Apr. 2023, Art. no. 3, doi: [10.37188/lam.2023.003](https://doi.org/10.37188/lam.2023.003).
- [117] C. Xiang et al., "High-performance silicon photonics using heterogeneous integration," *IEEE J. Sel. Topics Quantum Electron.*, vol. 28, no. 3, May/Jun. 2022, Art. no. 8200515, doi: [10.1109/JSTQE.2021.3126124](https://doi.org/10.1109/JSTQE.2021.3126124).
- [118] O. Marshall et al., "Heterogeneous integration on silicon photonics," *IEEE Proc.*, vol. 106, no. 12, pp. 2258–2269, Aug. 2018, doi: [10.1109/JSTQE.2021.3126124](https://doi.org/10.1109/JSTQE.2021.3126124).
- [119] D. Kohler et al., "Biophotonic sensors with integrated Si₃N₄-organic hybrid (SiNOH) lasers for point-of-care diagnostics," *Light: Sci. Appl.*, vol. 4, no. 3, Mar. 2021, Art. no. 64, doi: [10.1038/s41377-021-00486-w](https://doi.org/10.1038/s41377-021-00486-w).
- [120] C. Weimann et al., "Silicon-organic hybrid (SOH) frequency comb sources for terabit/s data transmission," *Opt. Exp.*, vol. 22, no. 3, pp. 3629–3627, Feb. 2014, doi: [10.1364/OE.22.003629](https://doi.org/10.1364/OE.22.003629).



Wolfgang Freude (Life Senior Member, IEEE) received the Dipl.-Ing. (M.S.E.E.) and Dr.-Ing. (Ph.D.E.E.) degrees in electrical engineering from the University of Karlsruhe, Karlsruhe, Germany, in 1969 and 1975, respectively. He is currently a Professor with the Institute of Photonics and Quantum Electronics and Distinguished Senior Fellow with the Karlsruhe Institute of Technology. He has authored and coauthored more than 330 publications, coauthored a book entitled *Optical Communications* (in German, Springer 1991), and authored or coauthored seven book chapters. His research interests include the area of optical and wireless high-data rate transmission, high-density integrated-optics with a focus on silicon photonics, photonic crystals, and semiconductor optical amplifiers. He is an Honorary Doctor with Kharkov National University of Radioelectronics, Kharkov, Ukraine, and a Member of VDE/ITG and OPTICA. Among other engagements, he was the General Chair of the committee "Photonic Networks and Devices" in the framework of the OPTICA (formerly OSA) Advanced Photonics Congress in 2022. He is an editorial board Member for the Springer Nature Journals *Light: Science & Applications* and *Scientific Reports*.



Alexander Kotz received the B.Eng. degree in electrical engineering from the Baden-Württemberg Cooperative State University Mannheim, Mannheim, Germany, in 2016, and the M.Sc. degree in electrical engineering and information technology from the Karlsruhe Institute of Technology, Karlsruhe, Germany, in 2019. He is currently working toward the Ph.D. degree with the Institute of Photonics and Quantum Electronics with his main area of research being hybrid waveguide structures on silicon and silicon nitride for electro-optic and sensing applications.



Hend Kholeif received the B.Sc. degree in communication systems engineering from Ain Shams University, Cairo, Egypt, in 2019, and the M.Sc. degree in optics and photonics from the Karlsruhe Institute of Technology, Karlsruhe, Germany, in 2022. She is currently working toward the Ph.D. degree with the Institute of Photonics and Quantum Electronics. Her research interest focuses on silicon organic hybrid modulators for microwave-to-optical transduction.



Adrian Schwarzenberger received the B.Sc. degree in medical engineering from Hochschule Mannheim and University Heidelberg, Germany, in 2017, and the M.Sc. degree in optics and photonics with the Karlsruhe Institute of Technology, Karlsruhe, Germany, in 2020. He is currently working toward the Ph.D. degree with the Institute of Photonics and Quantum Electronics. His research interest focuses on silicon organic hybrid modulators for applications in extreme environments.



Artem Kuzmin received the B.Sc. and M.Sc. degrees in applied physics and mathematics from the Moscow Institute of Physics and Technology, Dolgoprudny, Russia, in 2005 and 2007, respectively, and the Ph.D. degree in physics from the the Kotelnikov Institute of Radio-engineering and Electronics, Moscow, Russia, in 2011. Since 2013, he has been with the Karlsruhe Institute of Technology, Karlsruhe, Germany. His research interests include cryogenic photonics and electro-optic devices, development of sensitive superconducting transition-edge sensors, and hot-electron-bolometer mixers for terahertz applications, ultrafast THz detectors from high-temperature superconductors for studying coherent synchrotron radiation, superconducting nanowire single-photon detectors for the optical and infrared range and for application with superconducting resonators. In 2023, he joined the Institute of Microstructure Technology and the Institute of Photonics and Quantum Electronics.



Carsten Eschenbaum received the diploma and M.Eng. degree from the University of Applied Sciences, Kaiserslautern, Germany, and the Dr.-Ing. degree in 2016. In 2014, he became the Head of Sensor System Group, Light Technology Institute, Karlsruhe Institute of Technology (KIT), Karlsruhe, Germany. The focus of his work was the development of printed optoelectronic sensors. In 2019, he joined the Institute of Photonics and Quantum Electronics, KIT, heading the group working on hybrid photonic integrated circuits. Since 2021, he has been a CTO and co-founder

of SilOriX GmbH, developing SOH devices for optical communication.



Adrian Mertens received the Dipl.-Phys and Dr.-Ing. degrees in physics from the Karlsruhe Institute of Technology (KIT), Karlsruhe, Germany, in 2012 and 2016, respectively. During his postdoctoral work on organic electronics with KIT he investigated till 2019 fully printable optical sensor systems based on organic waveguides. He then switched topic and developed a transportable, low-cost and open-source “Sensorbox” to investigate the effect of soiling on solar panels in rural areas within the CEWAG Project, conducted at KIT together with the University of the Gambia. In 2021, he began to work on SOH-modulators. He is currently one of the three co-founders and CEO of the start-up SilOriX, which aims to commercialize this technology.



Sidra Sarwar received the B.Sc. and M.Sc. degrees in chemistry from Quaid-e-Azam University Islamabad, Islamabad, Pakistan and the Ph.D. degree, in molecular magnetism from the RWTH Aachen University and Forschungszentrum Jülich, Germany, in 2021. In 2017, she started her doctoral work. Since 2022, she has been a Postdoctoral Researcher with the Institute of Photonics and Quantum Electronics and Institute of Organic Chemistry, Karlsruhe Institute of Technology, Karlsruhe, Germany. Her research is focused on the synthesis of efficient and stable electro-optic materials for silicon-organic-hybrid modulators.



Peter Erk, born in Schweinfurt in 1960. He received the doctorate degree on “Conductive Radical Anion Salts” in chemistry from the University of Würzburg, Würzburg, Germany, in 1989. He was with the research organization of BASF SE from 1991 to 2020 and as Vice President since 2008. He is currently the Managing Director of erConTec GmbH, Wachenheim an der Weinstraße, Germany. He is author and co-author of more than 60 patent families and more than 90 scientific publications. He is a Member of German Bunsen Society and the Vice-Chairman in the board of the photochemistry division of the Gesellschaft Deutscher Chemiker.



Stefan Bräse received the Ph.D. degree in 1995 in Göttingen and studied chemistry in Göttingen, Bangor, and Marseille, respectively. After postdoctoral research with Uppsala and the Scripps Research, he began his independent research with the RWTH Aachen, Aachen, Germany, in 1997, and was promoted to Professor in Bonn in 2001. Since 2003, he has been a Professor with the Institute of Organic Chemistry, Karlsruhe Institute of Technology (KIT), Karlsruhe, Germany, and since 2012, he has been the Director of the Institute of Biological and Chemical Systems (ITG, now IBCS-FMS), KIT. His research interests include synthetic chemistry, molecular engineering of functional synthetic materials, and digitization in chemistry.



Christian Koos (Member, IEEE) received the Ph.D. (Dr.-Ing.) degree in electrical engineering from the University of Karlsruhe, Karlsruhe, Germany, in 2007. From 2008 to 2010, he was affiliated with Carl Zeiss AG, Oberkochen, Germany, where he led the technology radars “Nanotools and Nanometrology” and “Metrology” within the Corporate Research and Technology department. He is currently a Full Professor with the Karlsruhe Institute of Technology and the Director of the Institute of Photonics and Quantum Electronics and Institute of Microstructure Technology. Over the previous years, he has co-founded a series of start-up companies such as Vanguard Photonics GmbH, Vanguard Automation GmbH, SilOriX GmbH, Deeplight SA, and Luxtelligence SA. He is the author of more than 140 journal papers and more than 35 patent families. His research interests include silicon photonics and hybrid integration concepts along with the associated applications in high-speed communications, optical sensing and metrology, and ultra-fast photonic-electronic signal processing. He was the recipient of several research awards and prestigious grants, such as an ERC Starting Grant in 2011 and an ERC Consolidator Grant in 2017.